Data-Informed Inversion Model (DIIM): a framework to retrieve marine optical constituents in the BOUSSOLE site using a three-stream irradiance model

Carlos Enmanuel Soto López^{1,2}, Mirna Gharbi Dit Kacem^{1,2}, Fabio Anselmi¹, and Paolo Lazzari²

Correspondence: Carlos Enmanuel Soto López (carlos.soto362@gmail.com)

Abstract. Within the New Copernicus Capability for Trophic Ocean Networks (NECCTON) project, we aim to improve the current data assimilation system by developing a method for accurately estimating marine optical constituents from satellitederived Remote Sensing Reflectance. We developed and compared two frameworks by implicitly inverting based on the implicit inversion of a semi-analytical expression model derived from the classical Radiative Transfer Equation. First, we used a Bayesian estimation, which provided retrievals. The first approach employed an iterative Bayesian inversion with a Gaussian approximation, which provides Maximum A Posteriori (MAP) estimates of the optical constituents along with their uncertainties. Moreover, associated uncertainties. To improve the model performance, we optimized the model parameters using historical in-situ measurements together with from the BOUSSOLE buoy and a Markov Chain Monte Carlo (MCMC) algorithmto adjust the model parameters, we were able to reduce the root mean square, which reduced the Root Mean Square Error (RMSE) between the retrieved data and in-situ observations. Second, we and observed values. The second approach employed the Stochastic Gradient Variational Bayes (SGVB) framework to efficiently approximate the Maximum Posterior (MAP) estimator, which is designed to approximate the MAP estimates of the optical constituents while simultaneously finding the Maximum Likelihood Estimate (MLE) of the model parameters. This approach optimizing the model parameters through maximum likelihood. This method resulted in faster computations of the optical constituents compared to Bayesian estimations, with equivalent RMSE values between the retrieved data and than the iterative Bayesian inversion, while maintaining comparable RMSE values. While the iterative Bayesian inversion provided reliable uncertainty estimates, the SGVB estimator offered faster computations of the optical constituents. Moreover, using a dataset of in-situ observations. We showed that both, the MCMC and SGVB based algorithms, were able to find sets of optimal parameters, which, due to correlations between them, are not uniquesea surface chlorophyll-a concentrations across a broad region of the Northwestern Mediterranean Sea, we compared the inversion techniques with a state-of-the-art algorithm used within the Copernicus Marine Service, finding comparable performances across methods. Notably, the SGVB estimator showed the highest correlation between in-situ measurements and retrievals throughout the analyzed region. We conclude that both methods are consistent with the Radiative Transfer Equation. The first method provides reliable uncertainty estimations inversion methods achieve a performance comparable to existing state-of-the-art algorithms. The Gaussian approximation offers robust uncertainty quantification, while the second offers a faster alternative to standard inversion techniques, making it suitable for inversion and model

¹Università degli Studi di Trieste, 31127, Italy

²Istituto nazionale di oceanografia e di geofisica sperimentale - OGS, Trieste, 34010, Italy

optimization problems where MCMC algorithms are intractable SGVB estimator provides a reliable and computationally efficient alternative in marine sciences.

1 INTRODUCTION

40

Operational systems, like Copernicus, use satellite-derived data, combined with data assimilation techniques, to obtain estimates of the marine ecosystem status. Traditionally, the assimilated variable is the chlorophyll retrieved data; nowadays, state of the art biogeochemical models are progressively including refined bio-optical models able to simulate optical variables such as Remote Sensing Reflectance, enabling the direct assimilation of multispectral reflectance measured by satellite sensors.

In this work, we aim to derive a framework to estimate the ocean inherent optical properties (IOPs), such as absorption and scattering coefficients, from measurements of satellite-derived apparent optical properties (AOPs), like irradiance and Remote Sensing Reflectance. The IOPs are of interest in their own right, as they carry key information about ecosystem variables, such as chlorophyll, which can be used as indicators of the trophic condition of large marine areas (Longhurst et al., 1996). Most importantly, the framework is intended to be employed as a module in a data assimilation schemes scheme (Bruggeman et al., 2023), within an operational model services, to perform Remote Sensing Reflectance assimilation in a coherent way, providing an aligned forward and inverse procedure.

The retrieval of the IOPs of water bodies from measurements of the AOPs, is referred to as the inverse problem of ocean optics. This is crucially important since directly measuring IOPs with an extended spacial spatial coverage is very difficult (Gordon, 2002).

The first step to compute the IOPs is to establish the forward relationship between the AOPs and the IOPs. In this context, the AOPs are described as a function of the IOPs using the Radiative Transfer Equation (RTE). Due to the complexity of the RTE, this computation is carried out in simple scenarios, resulting in simplified equations that can be solved analytically. Other approaches involve using semi-analytical equations or empirical relations, where the latter are combined with simplified expressions of the RTE. The inverse problem is solved using these forward computations to estimate the IOPs either explicitly, by analytically inverting the forward process (Zaneveld, 1989; Leathers et al., 1999; Tao et al., 1994; McCormick, 1996; Stramska et al., 2000; Salama and Verhoef, 2015; Lazzari et al., 2024), or implicitly, by using an estimate of the IOPs in the forward process and then iteratively adjusting the IOP values to match measurements of the AOPs (Gordon and Boynton, 1997; Boynton and Gordon, 2000; Michalopoulou et al., 2009; Salama and Verhoef, 2015; Erickson et al., 2023; Leaders and Verhoef, 2015; Erickson et al., 20

In this work, we focused on an implicit inverse method, where the following Lazzari et al. (2024), but giving the method a probabilistic interpretation, allowing for the uncertainty estimation of the retrieved quantities. The forward model is the bio-optical model presented in Dutkiewicz et al. (2015) and described in section 2.1, a three-stream semi-analytical irradiance model. The IOPs from the bio-optical model are the absorption, scattering, and backward scattering coefficients of four optical-constituents optical constituents: water, chlorophyll- α (whose increase or decrease is associated with changes in the

density concentration of phytoplankton), Chromophoric Dissolved Organic Matter, and Non Algal Particles. We focused in finding the density on finding the sea surface concentration of these optical constituents, since we estimated the former IOPs as linear combinations of the latter. The model also depends on ad hoc parameters, originally computed as part of empirical relations from different studies (Morel, 1974; Aas, 1987; Dutkiewicz et al., 2015; Mason et al., 2016; Álvarez et al., 2023). We will optimize these parameters utilizing also optimized these parameters such that the retrieved quantities are accurate with respect to historical in-situ observations.

We compared two different frameworks. The first one is a Bayesian estimation, where we used a linearization of the forward process for estimating the uncertainties of the optical constituents, and Markov Chain Monte Carlo (MCMC) (Chib and Greenberg, 1995; Andrieu and Thoms, 2008) for the uncertainty of the parameters. This approach is described in section 4.

The second approach is based on Variational Bayes, by using the Stochastic Gradient Variational Bayes (SGVB) frameworkestimator, introduced by Kingma and Welling (2013), and described in section 4.4. Allows It allows for the estimation of parameters while also learning an estimate of the posterior distribution of the optical constituents. The idea is to approximate the probability distribution of the optical constituents given the satellite-derived Remote Sensing Reflectance using a neural network. This is the same framework used to train generative models known as Variational Auto Encoders (VAE), which also have have also been used to solve inversion problems (Zhong et al., 2019, 2021; Zhao et al., 2023; Shmakov et al., 2024). Originally proposed to solve inversion problems for cases when the posterior distribution is intractable (practically impossible to compute), this framework provides a fast way of estimating optical constituents, which are consistent with the forward model , and the in-situ observations.

We employed three data sources covering a time span period from 2005 to 2012: a A dataset of historical satellite-derived Remote Sensing Reflectance, a dataset from the Ocean–Atmosphere Spectral Irradiance Model (OASIM, used as boundary conditions for the bio-optical model (Gregg and Casey, 2009)), and a set of in-situ measurements from the BOUSSOLE buoy, located in the Ligurian basin of the northwestern Mediterranean Sea (coordinates 7.54°E, 43.22°N) (Antoine et al., 2008). The description of the different datasets is presented in section 3.

2 DATA ACQUISITION

65

1.1 Ocean-Atmosphere Spectral Irradiance Model (OASIM)

As explained in Gregg and Casey (2009), "the OASIM model is intended to provide the surface irradiance over the oceans with sufficient spectral resolution to support ocean ecology, biogeochemistry, and heat exchange investigations, and of sufficient duration to support inter-annual and decadal investigations." From this model, we used the surface downward direct irradiance, the surface photosynthetic available radiation, and the sun zenith angle, all for the coordinates at the BOUSSOLE buoy (Antoine et al., 2008), at wavelengths equal to 412.5, 442.5, 490, 510 and 555.

1.1 Satellite-derived Remote Sensing Reflectance

We used a Level 3 product provided by the E.U. Copernicus Marine Service Information (CMEMS). This is a merge of Level 2 Remote Sensing Reflectance from different satellite sources, as explain in Colella et al. (2023). This product provides pre-processed Remote Sensing Reflectance with daily resolution, spacial resolution of one kilometer, at six different wavelengths: 412, 443, 490, 510, 555 and 670. Due to the fact that for oligotrophic and mesotrophic water, the absorption of water for wavelengths higher than 555 is dominant over the other constituents (Lee et al., 2002), we focus our attention on the data with wavelength less or equal than 555. The values at the wavelengths 412 and 443 were assumed to be the same as the values with wavelengths at 412.5 and 442.5 in order to match the values computed with the OASIM model.

1.1 In-situ observations

We will use three sets of in-situ observations: chlorophyll- α , particulate backward scattering coefficient and downward light attenuation coefficient, acquired from the BOUSSOLE buoy (Antoine et al., 2008).

The three sets of measurements had 15 minutes resolution. We used only measurements between 10:00 and 14:00 GMT as representative. After filtering the data with an absolute tilt higher or lower than 10 degrees and dose reported at a depth more than 2 below the nominal values (4 and 9, depending on the instrument of measurement), we proceeded to average the daily values. Due to the noise in the measurements, before averaging, the downward light attenuation coefficient data was filtered with an analog high pass filter, using the package SeiPy (Virtanen et al., 2020) from the programming language Python (Van Rossum and Drake, 2009), also filtering the noise with a frequency less than 4 hours.

Due to low vertical variability, the measurements of chlorophyll- α and particulate backward scattering coefficient were considered as the values just above the water-air interface. The former one had measurements at wavelengths equal to 442, 488, 550 and 620.

Due to the height vertical variability of the downward light attenuation coefficient, the measurements were considered to be at a depth of 9, with values at the wavelengths 412, 442, 490, 510, 555, 560, 665, 670, 681.

For the same reasoning described in section 3.2, we only used the values less or equal than 555. The values at the wavelengths 412, 442, 488 and 550 were assumed to be the same as the values with wavelengths at 412.5, 442.5, 490 and 555 in order to match the values computed with the OASIM model.

2 BIO-OPTICAL MODEL

We now describe the Bio-optical model (Aas, 1987; Ackleson et al., 1994; Dutkiewicz et al., 2015; Álvarez et al., 2023), which details the interaction of the radiance with different constituents in the sea, called optical constituents. In section 2.1 we present the model of the water-leaving radiance, based on the classical Radiative Transfer Model (Dutkiewicz et al., 2015). In section 2.2, we use this model to compute the theoretical Remote Sensing Reflectance (R_{rs}^{MODEL}) (Aas and Højerslev, 1999). The aim of the inversion problem is inversion problem aims to use this model, named the forward model, and satellite measurements , to retrieve optical constituents that are consistent with future observations, for . For this end, we used historical in-situ observations described in section 2.3.

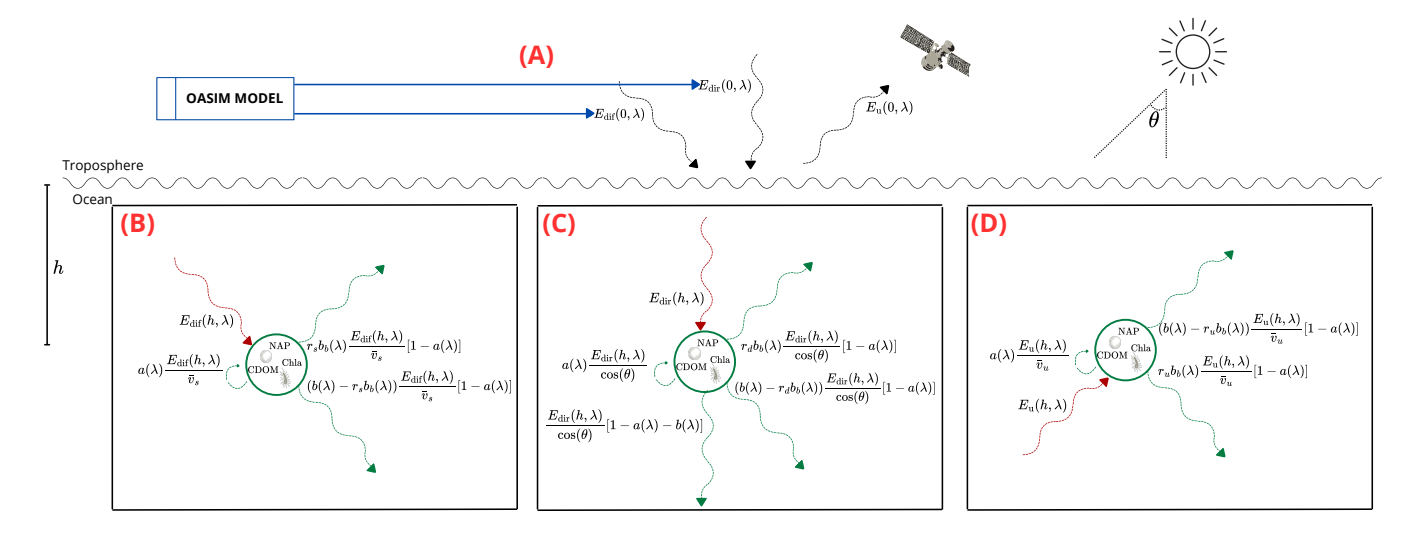


Figure 1. Diagram illustrating the main components of Eq. 1, showing: (A) the incoming irradiance (modeled using the OASIM model; see Sec. 3), and how it interacts with chlorophyll, non-algal particles, and colored dissolved organic matter (CDOM), leading to the attenuation and scattering of: (B) the diffuse, (C) direct, and (D) upward component into upward and downward fluxes.

2.1 Radiative Transfer Model

To simulate the water-leaving radiance, we followed Dutkiewicz et al. (2015), using a one-dimensional, three-stream radiance model, where the vertical component of the radiance over the water column is decomposed into three interacting components (see Fig. 1) following the system of equations,

$$\frac{dE_{\text{dir}}(h,\lambda)}{dh} = -\frac{a(\lambda) + b(\lambda)}{\cos\theta} E_{\text{dir}}(h,\lambda),$$

$$\frac{E_{\text{dif}}(h,\lambda)}{dh} \frac{dE_{\text{dif}}(h,\lambda)}{dh} = -\frac{a(\lambda) + r_s b_b(\lambda)}{v_s} E_{\text{dif}}(h,\lambda) + \frac{r_u b_b(\lambda)}{v_u} E_u(h,\lambda) + \frac{b(\lambda) - r_d b_b(\lambda)}{\cos\theta} E_{\text{dir}}(h,\lambda),$$

$$\frac{E_u(h,\lambda)}{dh} \frac{dE_u(h,\lambda)}{dh} = -\frac{r_s b_b(\lambda)}{v_s} E_{\text{dif}}(h,\lambda) + \frac{a(\lambda) + r_u b_b(\lambda)}{v_u} E_u(h,\lambda) - \frac{r_d b_b(\lambda)}{\cos\theta} E_{\text{dir}}(h,\lambda).$$
(1)

These three equations describe how the vertical direct irradiance $E_{\rm dir}(h,\lambda)$ is attenuated by absorption, with $a(\lambda)$ the total absorption coefficient, and scattered into downward $E_{\rm dif}(h,\lambda)$, and upward irradiance $E_{\rm u}(h,\lambda)$, $b(\lambda)$ the total scattering coefficient, $b_b(\lambda)$ the total backward scattering coefficient, r_d , r_s and r_u the effective scattering coefficients normalized with respect to the backward scattering coefficients, $\cos(\theta)$, v_s and v_u the average cosines of the irradiance components, θ the Sun zenith angle, h the depth, and λ the wavelength.

Following Dutkiewicz et al. (2015), the values for r_d , r_s , r_u , v_s and v_u are approximated as constants (see Table Tab. 2). See Dutkiewicz et al. (2015), appendix B, for a derivation starting from the classical radiative transfer equation. For previous

studies where similar transfer models have been used, see Aas (1987); Ackleson et al. (1994); Salama and Verhoef (2015); Álvarez et al. (2023) and Lazzari et al. (2024).

The total absorption and scattering coefficients are modeled as,

140

$$a(\lambda) = a_{w}(\lambda) + a_{phy}(\lambda) \text{chla} + a_{CDOM}(\lambda) \text{CDOM} + a_{NAP}(\lambda) \text{NAP},$$

$$b(\lambda) = b_{w}(\lambda) + b_{phy}(\lambda) C + b_{NAP}(\lambda) \text{NAP},$$

$$b_{b}(\lambda) = b_{b,W}(\lambda) + b_{b,phy}(\lambda) C + b_{b,NAP}(\lambda) \text{NAP},$$

$$(2)$$

with chla, NAP and CDOM the concentration of the optical constituents Chlorophyll- α , Non Algal Particles and Chromophoric Dissolved Organic Matter respectively; $a_{\rm w}(\lambda)$ is the water-specific absorption coefficient, $b_{\rm w}(\lambda)$ and $b_{b,\rm w}(\lambda)$ the water-specific scattering and backward scattering coefficients, $a_{\rm phy}(\lambda)$ the chlorophyll-specific absorption coefficient of phytoplankton, $b_{\rm phy}(\lambda)$ and $b_{b,\rm phy}(\lambda)$ the carbon-specific scattering coefficients of phytoplankton (see Table-Tab. 1), C the carbon concentration, which is derived as a function of chlorophyll and irradiance (Geider et al., 1997), with the chla:C ratio represented as a sigmoid curve dependent on Photosynthetic Available Radiation (PAR), as

$$C = \text{chla} / \left(\Theta_{\text{chla}}^{0} \frac{e^{-(\text{PAR} - \beta)/\sigma}}{1 + e^{-(\text{PAR} - \beta)/\sigma}} + \Theta_{\text{chla}}^{\min}\right), \tag{3}$$

with Θ_{chla}^0 , β , σ , $\Theta_{\text{chla}}^{\text{min}}$ constant parameters (see Table Tab. 2), and $a_{\text{CDOM}}(\lambda)$, $a_{\text{NAP}}(\lambda)$ and $b_{\text{NAP}}(\lambda)$ the mass-specific absorption and scattering coefficients for CDOM and NAP respectably (Álvarez et al., 2023). The latter are respectively (Álvarez et al., 2023), with the latter calculated as,

$$a_{\text{CDOM}}(\lambda) = d_{\text{CDOM}} e^{-S_{\text{CDOM}}(\lambda - 450)},$$

$$a_{\text{NAP}}(\lambda) = d_{\text{NAP}} e^{-S_{\text{NAP}}(\lambda - 440)},$$

$$b_{\text{NAP}}(\lambda) = e_{\text{NAP}} \left(\frac{550}{\lambda}\right)^{f_{\text{NAP}}},$$
(4)

with S_{CDOM} , d_{CDOM} , S_{NAP} , d_{NAP} , e_{NAP} , e_{NAP} , e_{NAP} constant parameters (see Tab. 2), and $b_{b,\text{NAP}} = b_{r,\text{NAP}}b_{\text{NAP}}$, with $b_{r,\text{NAP}}$ the backscattering ratio of NAP.

PAR was computed following Lazzari et al. (2020), as,

$$PAR = \frac{10^6}{N_A h c} \int_{400 \text{nm}}^{700 \text{nm}} (E_{\text{dif}}(0, \lambda) + E_{\text{dir}}(0, \lambda)) \lambda d\lambda$$
 (5)

with N_A the Avogadro's number, c the speed of light and h the plancks constant.

For the rest of this work, we assumed only one homogeneous layer with constant densities. For deep case 1 waters, like the one studied in the present work, during winter, the chlorophyll concentration in the first layer is approximately constant due to mixing (see Mignot et al. (2011), Fig. 1), while most of the downward irradiance comes from the first 10 to 20 meters (see

Table 1. Parameters dependent of λ used for the Radiative Transfer Model evaluation, with the water-specific absorption coefficient $a_{w}(\lambda)$ from Mason et al. (2016), the water-specific scattering and backward scattering coefficients $b_{w}(\lambda)$, $b_{b,w}(\lambda)$ with values interpolated from Morel (1974), the phytoplankton-specific absorption coefficient $a_{phy}(\lambda)$ an average of interpolated from the average values for picophytoplankton, nanophytoplankton, diatoms and dinoflagellates, collected of different phytoplacton functional types from literature in Álvarez et al. (2023)(Álvarez et al., 2023), and the carbon-specific scattering and backward scattering coefficients $b_{phy}(\lambda)$ $b_{b,phy}(\lambda)$ from Dutkiewicz et al., (2015)(Dutkiewicz et al., 2015).

λ [nm]	$a_{\rm w}(\lambda) [{\rm m}^{-1}]$	$b_{\rm w}(\lambda)~{\rm [m^{-1}]}$	$b_{b,w}(\lambda) [\mathrm{m}^{-1}]$	$a_{\rm phy}(\lambda) [{\rm m}^2 ({\rm mgChla})^{-1}]$	$b_{\mathrm{phy}}(\lambda) [\mathrm{m^2(mgC)^{-1}}]$	$b_{b,\mathrm{phy}}(\lambda) [\mathrm{m}^2 (\mathrm{mgC})^{-1}]$
412.5	0.00271	0.00535	0.002674	0.0340.03713	0.021020.00318	5.38E-053.25E-06
442.5	0.00574	0.00437	0.002184	0.040.04019	0.020220.00311	5.18E-053.30E-06
490 490.0	0.01460.01460	0.00284	0.001421	0.0280.02741	0.020540.00335	5.26E-053.41E-06
510 510.0	0.0330.03300	0.00247	0.001234	0.018 0.01981	0.02050.00347	5.25E-053.42E-06
555 555.0	0.06098	0.00167	0.000836	0.0090.00917	0.019070.00353	4.88E-053.39E-06

Simpson and Dickey (1981), Fig. 1 and Fig. 2). During summer, there is no mixing, but still there is a region of around 20 to 50 meters with constant chlorophyll concentrations, making the assumption justified.

with S_{CDOM} , d_{CDOM} , S_{NAP} , d_{NAP} , e_{NAP} , f_{NAP} constant parameters (see Table 2).

160 2.2 Remote Sensing Reflectance

We used the system of equations in Eq. (1), subject to the boundary conditions

$$E_{\text{dir}}(0,\lambda) = E_{\text{dir}}^{\text{OASIM}}(0,\lambda), E_{\text{dif}}(0,\lambda) = E_{\text{dif}}^{\text{OASIM}}(0,\lambda), E_{\text{u}}(\infty,\lambda) = 0, \tag{6}$$

with $E_{\text{dir}}^{\text{OASIM}}(0,\lambda)$, $E_{\text{dif}}^{\text{OASIM}}(0,\lambda)$, the direct and diffuse downward irradiance on the surface of the ocean. For this work, we used the values from the OASIM model (Gregg and Casey, 2009). By assuming an infinitely deep and homogeneous column of water (Ronald and Zaneveld, 1982), the system of equations can be solved analytically, with the final expression presented in Appendix A.

The Remote Sensing Reflectance $R_{rs}^{MODEL}(\lambda)$ can be computed from the solution $E_{\rm u}(0,\lambda)$ (Aas and Højerslev, 1999) as

$$R_{rs}^{MODEL}(\lambda) = \frac{\boldsymbol{E}_{u,\lambda}(0)}{Q(\theta) \left(\boldsymbol{E}_{\text{dir},\lambda}(0) + \boldsymbol{E}_{\text{dif},\lambda}(0)\right)}$$
(7)

with

170
$$Q(\theta) = Q_a e^{-Q_b \sin(\pi/180(90-\theta))},$$
 (8)

 Q_a and Q_b constant parameters (see Table Tab. 2).

Due to the interaction in the interface between the sea surface and the atmosphere, a correction has to be added to the R_{rs}^{MODEL} (Lee et al., 2002), with the relation,

$$\mathbf{R}_{rs,down}(\lambda) = \frac{R_{rs,up}(\lambda)}{T + \gamma R_{rs,up}(\lambda)} \tag{9}$$

Table 2. Parameters independent of λ used for the Radiative Transfer Model evaluation, r_d , r_s , r_u , v_s , v_u , S_{CDOM} , d_{CDOM} from Dutkiewicz et al. (2015) who take took them from Aas (1987), Θ_{chla}^0 , $\Theta_{\text{chla}}^{\min}$, σ β computed as an empirical model from data in the BOUS-SOLE Site (Lazzari et al., 2024), S_{NAP} , d_{NAP} , d_{NAP} , d_{NAP} and d_{TNAP} from (Álvarez et al., 2023) Álvarez et al. (2023), Q_a and Q_b from Aas and Højerslev (1999), and, T and γ from Lee et al. (2002).

Parameter name	Symbol	Value from literature	Units
Normalized effective scattering coefficient for direct irradiation	r_d	1.0	-
Normalized effective scattering coefficient for downward radiation,	r_s	1.5	-
Normalized effective scattering coefficient for backward radiation,	r_u	3.0	-
Average cosine for downward scattered radiation	v_s	0.83	-
Average cosine for upward scattered radiation	v_u	0.4	-
-	$\Theta^0_{ m chla}$	0.03	$mgChla(mgC)^{-1}$
-	$\Theta^{\min}_{ m chla}$	0.005	$mgChla(mgC)^{-1}$
-	σ	20	$(\mathrm{mmol})\mathrm{m}^{-2}\mathrm{s}^{-1}$
-	β	500	$(\mathrm{mmol})\mathrm{m}^{-2}\mathrm{s}^{-1}$
CDOM mass-specific absorption at 450 nm	$d_{ m CDOM}$	0.015	$m^2 (mgCDOM)^{-1}$
CDOM mass-specific absorption spectral slope between 350 and 500 nm	$S_{ m CDOM}$	0.017	nm
NAP mass-specific absorption at 440 nm	$d_{ m NAP}$	0.0013	$m^2 (mgNAP)^{-1}$
NAP mass-specific absorption spectral slope between 350 and 500 nm	$S_{ m NAP}$	0.013	nm
NAP mass-specific scattering at 550 nm	$e_{ m NAP}$	0.02875	$m^2 (mgNAP)^{-1}$
-	$f_{ m NAP}$	0.5	-
Backscattering-to-scattering ratio of NAP	$b_{NAP,R}b_{r,NAP}$	0.005	-
-	Q_a	5.33	-
-	Q_b	0.45	-
-	T	0.52	-
-	γ	1.7	-

where T and γ are constant parameters (see Table Tab. 2), $R_{rs,down}(\lambda)$ is the Remote Sensing Reflectance just under the sea surface, and $R_{rs,up}(\lambda)$ is the Remote Sensing Reflectance just up the sea surface.

Thus, the final expression for R_{rs}^{MODEL} is a model that depends on the optical constituents and the boundary conditions.

Since the Satellite Remote Sensing Reflectance measures are a merged product of many satellite samples (see Sec 3) during the day, the direct and diffuse downward irradiance on the surface of the ocean were computed as daily averages, only during hours with sun. For this reason, the densities involved in the computation of Eq. 7 are also daily averages.

180

2.3 Model of the in-situ observations

We aim to model the chlorophyll- α as the retrieved quantity from the inversion problem. The particulate backward scattering coefficient $(b_{b,p}(\lambda))$ is modeled as the contribution to backward scattering from the phytoplankton and NAP,

$$b_{b,p}(\lambda) = b_{b,\text{phv}}(\lambda)C + b_{b,\text{NAP}}(\lambda)\text{NAP}$$
(10)

where the carbon C is calculated as Eq. (3). The downward light attenuation coefficient (k_d) is computed by the relation,

$$E_{\text{dir}}(h,\lambda) + E_{\text{dif}}(h,\lambda) = (E_{\text{dir}}^{\text{OASIM}}(0,\lambda) + E_{\text{dif}}^{\text{OASIM}}(0,\lambda))e^{-k_d h}. \tag{11}$$

3 DATA ACQUISITION

3.1 Ocean-Atmosphere Spectral Irradiance Model (OASIM)

The OASIM model (Gregg and Casey, 2009) uses as input the claud, aerosol, and atmospheric conditions to simulate the propagation of light in the atmosphere, and return the irradiance at the surface of the ocean. We used the validated outputs for the BUOSSOLE site (Antoine et al., 2008) computed in Lazzari et al. (2020) as the boundary conditions in Eq. 6. The outputs are the surface downward direct irradiance E_{dir} and the surface downward scattered irradiance E_{dir}, from which the Photosynthetic Available Radiation PAR can be computed (Lazzari et al., 2020). The output from the model is in 33 wavelengths from 200 nm to 4 μm. As described in Lazzari et al. (2020), these values are further interpolated at wavelengths 412.5 nm, 442.5 nm,
 490 nm, 510 nm and 555 nm.

3.2 Satellite-derived Remote Sensing Reflectance

We used a Level 3 product provided by the E.U. Copernicus Marine Service Information (CMEMS). This is a merge of Level 2 Remote Sensing Reflectance from different satellite sources, as explained in Colella et al. (2023). This product provides pre-processed Remote Sensing Reflectance with daily resolution, spacial resolution of one kilometer, at six different wavelengths:

412 nm, 443 nm, 490 nm, 510 nm, 555 nm and 670 nm. Due to the fact that for oligotrophic and mesotrophic water, the absorption of water for wavelengths higher than 555 nm is dominant over the other constituents (Lee et al., 2002), we focus our attention on the data with wavelengths less than or equal to 555 nm. The values at the wavelengths 412 nm and 443 nm were assumed to be the same as the values with wavelengths at 412.5 nm and 442.5 nm in order to match the values computed with the OASIM model.

205 3.3 In-situ observations

We used three in-situ observations: chlorophyll- α , particulate backward scattering coefficient, and downward light attenuation coefficient, with data from the BOUSSOLE buoy (Antoine et al., 2008) retrieved as explained in Lazzari et al. (2024).

The three sets of measurements had 15 15-minute resolution. We used only measurements between 10:00 and 14:00 GMT as representative. First, we removed the data coming from the buoy if it reported an absolute tilt higher or lower than 10 degrees.

We also removed the ones reported at a depth more than 2 m below the nominal values (4 m and 9 m, depending on the instrument of measurement). Next, the downward light attenuation coefficient data were filtered with a Butterworth high-pass filter, using the package SciPy (Virtanen et al., 2020) from the programming language Python (Van Rossum and Drake, 2009), filtering the noise with a frequency less than 4 hours. Finally, we proceeded to average the daily values.

Due to low vertical variability, the measurements of chlorophyll-α and particulate backward scattering coefficient were considered as the values just below the water-air interface, even if the instruments were at 9 m deep. The former one had measurements at wavelengths equal to 442 nm, 488 nm, 550 nm, and 620 nm.

On the contrary, due to the high vertical variability of the downward light attenuation coefficient, the measurements were considered to be at a depth of 9 m, with values at the wavelengths 412 nm, 442 nm, 490 nm, 510 nm, 555 nm, 560 nm, 665 nm, 670 nm, 681 nm.

For the same reasoning described in section 3.2, we only used the values less than or equal to 555 nm. The values at the wavelengths 412 nm, 442 nm, 488 nm and 550 nm were assumed to be the same as the values with wavelengths at 412.5 nm, 442.5 nm, 490 nm and 555 nm in order to match the values computed with the OASIM model.

In other words, taking into account the previously said assumptions and data availability, the in-situ observations considered are sea surface chlorophyll, 9 meters deep downward light attenuation coefficient in 5 wavelengths, (412.5,442.5,490,510,555) nm, and sea surface particulate backward scattering coefficient at 3 wavelengths (442,490,510)nm.

4 BAYESIAN INVERSE PROBLEM

The model for the Remote Sensing Reflectance (R_{rs}^{MODEL}) depends on the density concentration of the optical constituents chla, NAP and CDOM. The inverse problem consists in of retrieving these constituents from the forward model , and the satellite observations (R_{rs}^{OBS}). In section–Sec. 4.1 we formalize the problem and introduce the nomenclature that is going to be used in the next sections, then in section–Sec. 4.2 and 4.3 we introduce the Bayesian approach to solve the problem (Rodgers, 2000), as well as the approach used to optimize the model.

4.1 Formal statement of the problem

We proceed to call $y \in \mathcal{Y}$ the set of wavelength-dependent satellite measurements, modeled with a forward model plus noise,

$$y(\lambda) = R_{rs}^{MODEL}(z, x(\lambda), \lambda; \Lambda) + \epsilon(\lambda), \tag{12}$$

235 where

225

230

$$x(\lambda) = (E_{\mathrm{dif}}^{\mathrm{OASIM}}(0,\lambda), E_{\mathrm{dir}}^{\mathrm{OASIM}}(0,\lambda), \theta, \mathrm{PAR})$$

are available simulated quantities, $x \in \mathcal{X}$, gathered from the OASIM model,

$$\begin{split} & \Lambda = & (r_s, r_u, r_d, v_s, v_u, a_{\text{w}}(\lambda), a_{\text{phy}}(\lambda), b_{\text{w}}(\lambda), b_{\text{phy}}(\lambda), b_{b, \text{W}}(\lambda), b_{b, \text{phy}}(\lambda), \\ & d_{\text{CDOM}}, S_{\text{CDOM}}, d_{\text{NAP}}, S_{\text{NAP}}, e_{\text{NAP}}, f_{\text{NAP}}, b_{NAP,Rr,\text{NAP}}, \Theta_{\text{chla}}^0, \Theta_{\text{chla}}^{\text{min}}, \beta, \sigma, Q_a, Q_b, T, \gamma), \end{split}$$

is athe set of parameters listed together with their literature values in Tab. 1 and Tab. 2, and

$$z = (\text{chla}, \text{NAP}, \text{CDOM})$$
 (13)

is at the set of unknown or latent quantities $z \in \mathcal{Z}$, which are the optical constituents.

The inverse problem aims to retrieve the unknown By performing the inversion, we compute an estimate of the unknown daily quantity z^d given a set of, which only depends in the measurements and OASIM-data $\{y_i^d, x_i^d\}_{i=0}^n$ performed during the day d, with n the number of measurements from the same day. Each day minimization is independent of the others, like screenshots of the state of the ocean, from which we aim to estimate the average concentrations of the active optical constituents.

Since we have measurements for a discrete set of wavelengths (at a depth h=0 m, with the exception of except k_d , at a depth h=9 m), the forward model is discretized as a five-dimensional vector, with each component representing values at different wavelengths. To distinguish between continuous functions and their respective discretization, λ is used as a subscript, e.g. $E_{dir,\lambda}$ represents a component of the five dimensional vector E_{dir} , with magnitudes $E_{dir}(0,\lambda)$, with were $\lambda = (412.5,442.5,490,510,555)$ nm. In similar fashion, $x_{\lambda} = (E_{dif,\lambda}, E_{dir,\lambda}, E_{u,\lambda}, \theta, PAR)$ $x_{\lambda} = (E_{dif,\lambda}, E_{dir,\lambda}, \theta, PAR)$ is a component of the 5×5 4 $\times 5$ tensor x. Using this notation, the measurements and OASIM-data of the day d are written as (y^d, x^d) .

Noise The noise ϵ is added to the model to account for the measurement uncertainty and the discrepancy between the forward model and the actual underlying function that governs the process, referred to as model uncertainty different sources of uncertainty. In this work, we assumed that ϵ is a random Gaussian variable with mean zero, and covariance Σ_{ϵ} .

As a consequence, the model of the measurement is a random variable with a Gaussian probability distribution

$$y \sim p_{\Lambda}(\boldsymbol{y}|z,\boldsymbol{x}) = \mathcal{N}(\boldsymbol{R}_{rs}^{MODEL}(z,\boldsymbol{x};\Lambda), \Sigma_{\epsilon}). \tag{14}$$

4.2 Bayesian approach to retrieve the latent variable

245

250

255

270

Under the Bayesian framework (Rodgers, 2000), the probability of the unknown quantity z, p(z|y, x), given the true probability distribution of the measurement p(y|z, x), can be retrieved using the Bayes theorem,

$$p(z|\mathbf{y}, \mathbf{x}) = \frac{p(\mathbf{y}|z, \mathbf{x})p(z|\mathbf{x})}{p(\mathbf{y}|\mathbf{x})}.$$
(15)

The probability distribution p(z|y,x) is called the posterior probability distribution, or just the posterior, p(y|z,x) the likelihood, and p(z|x) the prior probability distribution, or just the prior.

Since we are dealing with random variables, computing the posterior is equivalent to retrieving z. In the case when this computation is not possible, common approaches attempt to estimate the value of z that maximizes the posterior, named Maximum A-Posterior A Posterior (MAP) estimate.

In the case of little knowledge of the value of z, it is common practice to use an improper prior, p(z|x), as an uninformative prior, where each value of z is equally probable. This approach gives rise to With this choice of prior, the MAP is equivalent to finding the Maximum Likelihood Estimate (MLE).

Table 3. Root Mean Square Difference (RMSD) between in-situ measurements and the satellite measurements of R_{rs} in the Mediterranean Sea, obtained from a validation of the Copernicus Dataset (Colella et al., 2023).

$R_{rs,\lambda}$	$RMSD(R_{rs,\lambda})$
$R_{rs,412.5}$	$1.5 \times 10^{-3} \text{ sr}$
$R_{rs,442.5}$	$1.2 \times 10^{-3} sr$
$R_{rs,490}$	$1 \times 10^{-3} \text{ sr}$
$R_{rs,510}$	$8.6 \times 10^{-4} \text{ sr}$
$R_{rs,555}$	$5.7 \times 10^{-4} \text{ sr}$

For $\underline{\text{In}}$ this work, we used a log-normal distribution prior (Campbell, 1995) for the latent variable z, with parameters μ_z, Σ_z . This is equivalent to making the change of variable $\tilde{z} = \log(z)$ with a Gaussian prior with mean μ_z and covariance Σ_z . With this prior, and the Gaussian likelihood which can be derived from the forward model R_{rs}^{MODEL} , we can define the loss function

$$\mathcal{L}^{z,d}(\boldsymbol{y}^{d},\boldsymbol{x}^{d},\tilde{z}^{d};\Lambda) = -2\log(p_{\Lambda}(\tilde{z}^{d}|\boldsymbol{y}^{d},\boldsymbol{x}^{d}))$$

$$= (\boldsymbol{y}^{d} - \boldsymbol{R}_{rs}^{MODEL}(e^{\tilde{z}^{d}},\boldsymbol{x}^{d};\Lambda))^{T} \Sigma_{\epsilon}^{-1} (\boldsymbol{y}^{d} - \boldsymbol{R}_{rs}^{MODEL}(e^{\tilde{z}^{d}},\boldsymbol{x}^{d};\Lambda)) + (\tilde{z}^{d} - \mu_{z})^{T} \Sigma_{z}^{-1} (\tilde{z}^{d} - \mu_{z}) + c_{0}$$

$$(16)$$

with c_0 a constant. It can be shown that minimizing the loss function in Eq. (16), is the same as maximizing the posterior (Rodgers, 2000). In other words, We are interested in finding the \tilde{z}^d that minimizes this loss function, as an estimate of the true value for the optical constituents (under the log-normal assumptions).

As an estimate of Σ_{ϵ} , we used a diagonal matrix, with elements equal to the square of the Root Mean Square Difference (RMSD) between in-situ measurements and the satellite measurements of R_{rs} in the Mediterranean Sea, shown in Table Tab. 3, obtained from a validation of the Copernicus Dataset (Colella et al., 2023). This choice for Σ_{ϵ} is equivalent to assuming independence between measurements y_{λ}^{d} with different wavelengths.

For the prior parameters, we used $\mu_z = 0$ and $\Sigma_z = 1 * \alpha \Sigma_z = 1 \alpha$, with 1 a diagonal matrix of dimension 3×3 , and α a hyperparameter to be determined. These parameters were chosen in order to recover the This choice of Σ_z is equivalent to a ℓ_2 regularization. In Appendix B we explain the criteria used to tune α .

To retrieve $\tilde{Z}^* = \{\tilde{z}^{d*}\}_{d=1}^D$, the MAP estimate of the latent variable \tilde{z} for each day d, we want to minimize $\mathcal{L}^{z,d}$ with respect of \tilde{z}^d for every day d. We can perform this retrieval for all the historical data by minimizing the loss function,

$$\tilde{Z}^* = \operatorname{argmin}_{\tilde{Z}} \mathcal{L}^z
= \operatorname{argmin}_{\tilde{Z}} \sum_{d=0}^{D} \mathcal{L}^{z,d}(\boldsymbol{y}^d, \boldsymbol{x}^d, \tilde{z}^d; \Lambda).$$
(17)

4.3 Model optimisation scheme

280

285

We want to optimize the forward model $\mathbf{R}_{rs}^{MODEL}(\tilde{z}, \mathbf{x}^d; \Lambda)$ by adjusting the parameters Λ , using the in-situ observations $H^{OBS} = \{(\mathbf{k}\mathbf{d}^{d,\text{obs}}, \mathbf{b_{bp}}^{d,\text{obs}}, \text{chla}^{d,\text{obs}})\}_{d=1}^{D}$, where D is the number of days, $\mathbf{k}\mathbf{d}^{d,\text{obs}}$ is a vector of dimension five, $\mathbf{b_{bp}}^{d,\text{obs}}$ as

vector of dimension three given that there are only in-situ observations for $\lambda = (442.5, 490, 555)$ nm, and $chla^{d,obs}$ a scalar. Therefore, H^{OBS} is a set of nine dimensional vectors defined for each day.

In order to take into account missing data, we introduce the modeled observation function, H^{MODEL} , a nine dimensional vector analogous to H^{OBS} , and the presence-absence nine dimensional vectors I^d , with components equal to one if there are observations and zero otherwise.

Finally, we defined \mathcal{H} as the scalar product between I^d and H^{MODEL} for each day,

$$\begin{split} \underline{\mathcal{H}(Z, \boldsymbol{X}; \boldsymbol{\Lambda})} &= \{I^d \cdot H^{\text{MODEL}}\}_{d=1}^D \\ &= \{I^d \cdot (\boldsymbol{k}\boldsymbol{d}(z^d; \boldsymbol{x}^d, \boldsymbol{\Lambda}), \boldsymbol{b_{bp}}(z^d; \boldsymbol{x}^d, \boldsymbol{\Lambda}), \text{chla})\}_{d=1}^D \end{split}$$

where
$$Z = \{z^d\}_{d=1}^D$$
 and $X = \{x^d\}_{d=1}^D$.

We aim to optimize the parameters Λ from the estimated probability distribution $p_{\Lambda}(y|z,x)$, by finding the Maximum Likelihood estimate of the parameters, given the in-situ observations. Using a Gaussian Likelihood with unitary covariance, we arrive to an expression for the negative log likelihood equivalent to a ℓ_2 norm,

$$\underline{\mathcal{L}^H = \frac{\sum_{d=0}^{D} ||\mathcal{H}^d(Z^*; \boldsymbol{X}, \Lambda) - H^{OBS, d}||_2}{D}}.$$

where $||\cdot||_2$ is the ℓ_2 norm, taken over a space with a dimension equal to the number of observations performed during a day 305 d. Minimizing this loss function would be equivalent to finding the Maximum Likelihood Estimate, but instead, in order to have an estimate of the uncertainty, we proceed to use a Markov State Monte Carlo algorithm to approximate the posterior probability distribution.

4.3 Optimization algorithm and Markov State Monte Carlo

We aim to use an algorithm that can estimate the latent variable z and his uncertainty, in an operationally efficient way. To do so, in the next section we describe how we minimized the loss function \mathcal{L}^z described in section 4.2, which is equivalent to finding the MAP estimate.

The final posterior distribution is not a Gaussian distribution, given that the forward model is a nonlinear function of z. Instead, to estimate his uncertainty in an operationally efficient manner, we approximated the posterior distribution with a Gaussian by linearizing the forward function around the MAP estimate.

In contrast, since the estimation of the mean and uncertainty of the parameters A is not intended to be part of an operational system, we approximate the posterior by using a Markov State Monte Carlo Algorithm described in section 4.3.1.

4.2.1 Estimation of the latent variable

We performed the

4.2.1 Estimation of the latent variable posterior

We performed the minimization of \mathcal{L}^z using the Adam algorithm, with a learning rate of 0.03 and all the default $\gamma = 0.03$, and $\beta_1 = 0.9$, $\beta_2 = 0.999$, which are the default momentum parameters from the library PyTorch (Paszke et al., 2019), with version 2.4.1. We used 90% of all the historical data per iteration, selected randomly across the entire time spanperiod. The remaining 10% was used as the test set. A copy of the code availability for every algorithm described in this work is in Soto (2025).

After \tilde{Z}^* , the set of latent variables for the entire training set, has been retrieved, in order to estimate the uncertainty, we linearized $R_{rs}^{MODEL}(e^{\tilde{z}^d}, x; \Lambda)$ around \tilde{z}^{d*} , as

$$\mathbf{R}_{rs}^{MODEL}(e^{\tilde{z}^{d}}, \mathbf{x}; \Lambda)$$

$$\approx \mathbf{R}_{rs}^{MODEL}(e^{\tilde{z}^{d*}}, \mathbf{x}; \Lambda) + \nabla_{\tilde{z}^{d}} \mathbf{R}_{rs}^{MODEL}(e^{\tilde{z}^{d}}, \mathbf{x}; \Lambda)|_{(\tilde{z}^{d} = \tilde{z}^{d*})} (\tilde{z}^{d} - \tilde{z}^{d*})$$

$$= \mathbf{R}_{rs}^{MODEL}(e^{\tilde{z}^{d*}}, \mathbf{x}; \Lambda) + \mathbf{K}(\tilde{z}^{d} - \tilde{z}^{d*}).$$
(18)

Where K is the Jacobian of $R_{rs}^{MODEL}(e^{\tilde{z}^{d*}}, x; \Lambda)$ with respect of \tilde{z}^d . Then, as shown in (Rodgers, 2000), the covariance matrix of the approximate posterior can be written as

330
$$\Sigma_{\tilde{z}^{d*}} = (\boldsymbol{K}^T \Sigma_{\epsilon}^{-1} \boldsymbol{K} + \Sigma_{z}^{-1})^{-1}.$$
 (19)

In this way, the uncertainty standard deviation is computed as the root square of the diagonal elements $\sigma_{\tilde{z}}$ of $\Sigma_{\tilde{z}^{d*}}$.

Then, since the resulting retrieved values \tilde{Z}^* are normally distributed, $Z^* = \exp(\tilde{Z}^*)$ has a log-normal distribution and thus, the uncertainty can be computed with the 68% confidence interval (here we match the convention of using the standard deviation as uncertainty for variables with normal distribution).

The uncertainty for derived variables like kd and $b_{b,p}$ is computed with standard error propagation (Arras, 1998), i.e. $\Delta F(x)^2 = \nabla_x F(x) \Sigma^x \nabla_x F(x)^T$, where $\Delta F(x)$ is the error of a function F(x), $\nabla_x F(x)$ is the Jacobian, and Σ^x is the covariance matrix of x, in our case, $\Sigma^x = \Sigma_{\bar{x}d^*}$. These equations assume that each component of x is not correlated with the others, and is only an approximation for nonlinear functions.

The previous procedure is equivalent to estimating the latent variable posterior with a log-normal distribution. A comparison of the true posterior and the estimated posterior can be appreciated in Figure 7, where the true posterior was computed by sampling using the Metropolis-Hasting Algorithm (see Algorithm 2). The discrepancy between the mean and standard deviation is due to the linearization step in Eq. 18. Algorithm 1 summarizes the steps used for the posterior estimate.

4.3 Model optimisation scheme

340

We retrieved the latent variable posterior in order to accurately estimate the daily average of chlorophyll, Non-Algal particles, and Colored Dissolved Organic Matter concentrations. To asses the accuracy of the inversion, we used the in-situ observations $H^{OBS} = \{(kd^{d,obs}, b_{bp}^{d,obs}, chla^{d,obs})\}_{d=1}^{D} \text{ where } D \text{ is the number of days with observations available, } kd^{d,obs} \text{ is a vector of dimension five containing daily in-situ observations of the downward light attenuation coefficient, } b_{bp}^{d,obs} \text{ is a vector of } d$

Algorithm 1 Algorithm for estimating the daily posterior estimate of the unknown latent variable z^d , and the derived quantities kd^d and b_{bp}^d :

Input: x^d , y^d .

- 1. Find $\tilde{z}^{d*} = \operatorname{argmin}_{zd} \mathcal{L}^{z,d}(\boldsymbol{y}^d, \boldsymbol{x}^d, \tilde{z}^d; \Lambda)$ using a minimization algorithm (For example, Adam).
- 2. Compute K, the Jacobian of $R_{Ts}^{MODEL}(e^{\tilde{z}^{d*}}, x; \Lambda)$ with respect of \tilde{z}^{d} .
- 3. Compute the covariance matrix of the approximate posterior as $\sum_{zd*} = (K^T \sum_{\epsilon}^{-1} K + \sum_{z}^{-1})^{-1}$.
- 4. The MAP estimate of the latent variable is equal to $z^{d*} = e^{z^{d*}}$. The uncertainty can be found by computing the 68% confidence interval of the log normal distribution. For this work, only the diagonal elements of $\Sigma_{z^{d*}}$ were used, assuming independence between the latent variables.
- 5. Use Eq. 10 and Eq. 11 to compute b_{bp}^d and kd^d respectively, and use standard error propagation for their uncertainties.

dimension three with observations of particulate backward scattering coefficient, only for the wavelengths $\lambda = (442.5, 490, 555)$ nm, and $chla^{d, obs}$ is a scalar observation of sea surface chlorophyll concentration.

By comparing the modeled observation operator $H^{\text{MODEL}} = (kd(z^d; x^d, \Lambda), b_{bp}(z^d; x^d, \Lambda), \text{chla})$ with the daily observations, we aimed to optimize the forward model $R^{MODEL}_{rs}(\tilde{z}, x^d; \Lambda)$ by adjusting the parameters Λ . We looked for Λ^* such that $\sum_{d=1}^{D} ||H^{\text{MODEL}}(z^{d*}; x^d, \Lambda^*) - H^{\text{OBS}}||$ is minimized, for some suitable choice of distance. Since not every day has observations available, and also occur that the observations corresponding to some of the wavelengths is missing, we worked with daily vectors with dimension equal to the total number observations available, e.g. days with all observations available correspond with vectors of dimension nine (five for kd^d , three for b_{bp} and one for chla), while days with less observations correspond to lower dimensional vectors.

Since we also want to estimate the uncertainty of the retrieved parameters, we used the standard deviation over all the train data as a measure of the spread of each observation, and defined the loss function,

$$\mathcal{L}^{H} = \sum_{d=0}^{D} \frac{\left(\mathbf{H}^{\text{MODEL},d}(Z^{*}; \boldsymbol{X}, \boldsymbol{\Lambda}) - H^{OBS,d}\right)^{2}}{\sigma_{\text{OBS}}^{2}}$$
(20)

where σ_{OBS} is the standard deviation of the observations computed only with the train data. We want to minimize this loss function and get an estimate for the uncertainty of the retrieved parameters. For this aim, we proceed to use a Markov State Monte Carlo algorithm, described in the next section.

4.3.1 Markov State Chain Monte Carlos Carlo algorithm for optimizing the model parameters

In order to estimate the posterior distribution of the parameters, $p(\Lambda|H^{\text{OBS}}, \hat{Z}, X)$, we used the Metropolis-Hasting Algorithm (Chib and Greenberg, 1995; Andrieu and Thoms, 2008). This approach

The algorithm returns samples from a probability density function $\pi(x)$ by defining a transition probability, Markov process with transition probability p(x,y) of moving from state x to state y. It can be shown that by a suitable definition of this transition probability, the Markov state process can converge asymptotically to the target distribution $\pi(x)$. The Metropolis-Hasting

Algorithm uses the transition probability

$$p(x,y) = q(x,y)\alpha(x,y), \underline{x \neq y}_{\sim}\alpha(x,y) = \min \left[\frac{\pi(y)q(y,x)}{\pi(x)q(x,y)}, 1\right] \underline{\text{if } \pi(x)q(x,y) > 0, = 1, \text{ otherwise}}$$
 (21)

where q(x,y) is the transition probability from x to y proposal transition probability, and $\alpha(x,y)$ is the probability of moving acceptance probability. With this definition, a sampling samples from $\pi(x)$ is performed by , first selecting an initial state can be drawn by following Algorithm 2.

Algorithm 2 Metropolis-Hasting Algorithm (Chib and Greenberg, 1995; Andrieu and Thoms, 2008). It consists in defining a Markov process. It is useful to sample from a target distribution $\pi(x)$ without knowing the normalization constant.

Define: Proposal transition probability q(x,y).

Input: Length L_{chain}.

Initialize: x_0 .

- 1. $x = array of length L_{chain}$.
- 2. $x[0] = x_0$, then computing the probability $\alpha(x_0, x_1)$ of moving to a new state x_1 sampled with a probability density $q(x_0, x_1)$. If.
- 3. For i=0 to i = $L_m 1$ do
 - 1. Sample a proposed new point $y \sim q(x[i], y)$.
 - 2. Compute $\alpha(x[i], y)$ as stated in Eq. 21.
 - 3. Sample a random number from a uniform distribution between 0 and 1. If the output is smaller than $\alpha(x[i], y)$ x[i+1] = y else x[i+1] = x[i].
- 4. Discard the first samples (reaching the asymptotical behaviour) and the movement is performed, then we sample the new state x_{\perp} and repeat the process with the new state as the original state, if the movement is not performed, then we sample the original state and repeat the process, correlated ones.

Some drawbacks are knownfor this algorithm, for example, the iterations have to be performed multiple times before the algorithm converges close to the mode of the distribution to its asymptotical behaviour, or that successive iterations are tend to be strongly correlated, so many iterations have to be performed in order to obtain uncorrelated samples. These difficulties get increasingly stronger increase as the dimensionality of the sampling space gets biggerhigher. In our case, to mitigate some of these effects, we choose to perturbed our parameters in such a way that we end up with a fourteen dimensional spacedidn't perturb all the parameters, leaving those that are more precisely measured in the literature unperturbed, like the water-specific absorption and scattering coefficients.

A further complication is that the probability density that we want to sample depends on Z^* , the latent variable. This means that, each time we want to do an iteration of the Metropolis-Hasting Algorithm, we would need to find the MAP estimate of Z, increasing the computational time. To mitigate this problem, we proceed to use an estimate \hat{Z} , consisting of a few iterations towards the MAP estimate.

Our model for the negative $\frac{\log likelihood}{\log likelihood}$ is the loss function \mathcal{L}^H described in 4.3, which give us the expression for the Likelihood

$$p(H^{OBS}|\Lambda, \hat{Z}, \boldsymbol{X}) \propto e^{-\frac{1}{2}\mathcal{L}^{H}(H^{OBS}, \hat{Z}, \boldsymbol{X}, \Lambda)}.$$
 (22)

The density function, $\pi(x)$, that we want to sample from $\dot{\tau}$ is the posterior probability for the parameters. By using an improper prior, using the Bayes theorem, substituting the optimal Z^* with an approximation \hat{Z} , and using a symmetric probability $q(\Lambda_i, \Lambda_j) = \mathcal{N}(\Lambda_i, \alpha_q \times 1)$, we arrive to the transition probability,

$$p(\Lambda_i, \Lambda_j) = \min \left[e^{-\frac{1}{2} \left(\mathcal{L}^H(H^{OBS}, Z^*, \boldsymbol{X}, \Lambda_j) - \mathcal{L}^H(H^{OBS}, Z^*, \boldsymbol{X}, \Lambda_i) \right)}, 1 \right],$$

390

415

a uniform prior, and $q(\Lambda_i, \Lambda_j) = \mathcal{N}(\Lambda_i, \alpha_q \mathbb{1})$, where α_q is a hyperparameter, whose value is important for the convergence speed, equal to the standard deviation of the distance between steps. We compute the acceptance probability as

$$\alpha(\Lambda_i, \Lambda_j) = \min \left[e^{-\frac{1}{2} \left(\mathcal{L}^H(H^{OBS}, \hat{Z}, \mathbf{X}, \Lambda_j) - \mathcal{L}^H(H^{OBS}, \hat{Z}, \mathbf{X}, \Lambda_i) \right)}, 1 \right]. \tag{23}$$

The perturbation of the parameters was performed in a non-standard way, since all the parameters Λ have an interpretation in the forward model. Consequently, Regarding the perturbed parameters, we consider the literature values Λ^0 as close estimations estimates of the optimal values and look for a set of parameters ones. For this reason, we perturbed them as $\Lambda^* = \delta_{\Lambda}^T \Lambda^0$, where δ_{Λ} is a vector of small perturbations from the unity unity, referred to as perturbation factors.

In order to preserve the shape of the absorption of chlorophyll as a function of the wavelength $a_{phy}(\lambda)$, the vector The values of the λ dependent vector of dimension five representing the phytoplacton-specific absorption coefficients a_{phy} was perturbed as $a_{phy}^* = \delta_{a_{phy}} a_{phy}^0$, with $\delta_{a_{phy}}$ a learnable scalar and a_{phy} , and a_{phy}^0 , the literature values. The scattering coefficient of chlorophyll We chose it like this to maintain the shape of the function $a_{phy}(\lambda)$ unperturbed.

For the carbon-specific scattering and backscattering coefficients $b_{phy}(\lambda)$ was approximated as a linear function of λ , so we and $b_{b,phy}(\lambda)$, we first linearly interpolated them with the literature values, and perturbed the tangent and the intercept of the linear interpolation. The backward scattering coefficient $b_{b,phy}(\lambda)$ was perturbed in the same manner. The interpolations, $b_{phy}(\lambda)^* = \delta_{b_{phy}, hy} b_{phy}^0 + \delta_{b_{phy}, hy} b_{phy}^0 + \delta_{b_{phy}, hy}^0 +$

The parameters d_{CDOM} , $b_{NAP,R}b_{\text{CNAP}}$, S_{CDOM} , $\Theta_{\text{chla}}^{\min}$, Θ_{chla}^0 , β , σ , Q_a and Q_b perturbations consisted in a per parameter scalar multiplication multiplications. All the other parameters were left unperturbed.

In this way, we perturbed 24 parameters, 9 of them by multiplying them for a scalar δ_i , i equal to each of the perturbed parameters, the five components of a_{phy} by multiplying them by the same scalar $\delta_{a_{\text{phy}}}$, and finally, $b_{\text{phy}}(\lambda)$ and $b_{b,\text{phy}}(\lambda)$ by linearly interpolating them, and perturbing the tangent and the intercept of each of them, making a total of 14 perturbation factors.

In this manner, the perturbations δ_{Λ} were initialized with ones, then using alternate minimization (AM), alternating between finding the MAP estimate of Z^* and the MLE of the parameters, we reach values for δ_{Λ} that we expected were close to the mode of the posterior. Next. Finally, we used the Metropolis-Hasting Algorithm, waiting until the mean value of the different

parameters converged. Since consecutive samples are strongly correlated, we compute the length such that consecutive samples weren't strongly correlated, in our case, two hundred and eighty iterations to estimate the posterior, as described in Algorithm 3.

Algorithm 3 Metropolis-Hasting Algorithm with alternate minimization. Here we expand the Metropolis-Hasting Algorithm in combination with the alternate minimization to sample from the posterior probability of the parameter space

Define: Transition probability $q(\Lambda_i, \Lambda_i) = \mathcal{N}(\Lambda_i, \alpha_g \mathbb{1})$.

Input: L_{chain} (Lenghts of mcmc chaing), N_{steps} (Number of AM steps), $N_{\text{z_steps}}$ (steps towards the min of z^*).

Initialize: Λ_0 as the literature values.

- 1. Alternate minimization to estimate the MLE of the parameters. Finally, we ran forty times the Metropolis-Hasting Algorithms, with random initializations, close to the AM output. For each of them, we drop the first two thousand iterations to ensure convergence,
 - 1. For i=0 to $i=N_{\text{steps}}$ do
 - Find an estimate of all the latent variables $\hat{Z}^* \approx \operatorname{argmin}_{\tilde{z}} \mathcal{L}^z(\boldsymbol{y}, \boldsymbol{x}, \tilde{z}; \Lambda_0)$ by performing $N_{z \text{ steps}}$ iterations towards the minimum of the loss function.
 - Perform one step towards the minimization of $\mathcal{L}^{H}(y,x,\hat{Z}^{*};\Lambda_{0})$, and set Λ_{0} to the new value.
- 2. Define an empty array Λ of length L_{chain} .
- 3. $\Lambda[0] = \Lambda_0$.

420

- 4. For i=0 to i = $L_{\text{chain}} 1$ do
 - 1. Sample a proposed new point $\Lambda_i \sim \mathcal{N}(\Lambda[i], \alpha_q \mathbb{1})$.
 - 2. Find an estimate of all the latent variables $\hat{Z}^* \approx \operatorname{argmin}_{\bar{z}} \mathcal{L}^z(y, x, \tilde{z}; \Lambda_j)$ by performing a finite amount of iterations towards the minimum of the loss function.
 - 2. Compute $\alpha(\Lambda_i, \Lambda_j)$ as stated in Eq. 23 using the estimate \hat{Z}^* instead of the true minimum Z^* .
 - 3. Sample a random number from a uniform distribution between 0 and sampled only non correlated values. 1. If the output is smaller than $\alpha(\Lambda_i, \Lambda_j)$, make $\Lambda[i+1] = \Lambda_j$ else $\Lambda[i+1] = \Lambda[i]$.
- 5. Discard the first samples (reaching the asymptotical behaviour) and the correlated ones.
- 4.4 Neural Network Based Inversion Method: Data Informed Inversion Method (DIIM): A Variational Bayes approach

As the dimension of the posterior increases, MCMC methods became become increasingly more challenging, and even point-ways point-wise estimates, like the one obtained with Alternate Minimization, could not converge, due to the non convexity nonconvexity of our models. As an alternative approach, we present a framework based on the Stochastic Gradient Variational Bayes (SGVB) framework estimator (Kingma and Welling, 2013).

The SGVB based framework considers a random latent variable $z \in \mathcal{Z}$ sampled from an unknown distribution $p_{\Lambda^*}(z)$, and a random variable $y \in \mathcal{Y}$ sampled from a distribution $p_{\Lambda^*}(y|z)$ conditional on the latent variable z. For example, y could be measurements from a known physical process, conditional on unknown physical hidden processes.

The aim is to efficiently approximate the Maximum Marginal Likelihood estimate of the parameters Λ ,

$$\Lambda^* = \operatorname{argmax}_{\Lambda}(p_{\Lambda}(y)). \tag{24}$$

For this end, the posterior probability distribution $p_{\Lambda}(z|y)$ is estimated as a parameterized function $q_{\phi}(z|y)$. It can be shown that finding Λ^* and ϕ^* such that

$$\Lambda^*, \phi^* = \underset{\Lambda}{\operatorname{argminargmax}}_{\Lambda, \phi} \mathcal{L}_{ELBO},$$

435

440

$$\mathcal{L}_{ELBO} = -D_{KL}(q_{\phi}(z|\mathbf{y})||p_{\Lambda}(z)) + \mathbb{E}_{q_{\phi}(z|\mathbf{y})}[\log(p_{\Lambda}(\mathbf{y}|z))]$$
(25)

were where $D_{KL}(\cdot||\cdot)$ is the Kullback-Leibler divergence (DK-DKL divergence), an asymmetric, positively defined measure of the proximity between two probability distributions (Shlens, 2014), $p_{\Lambda}(z)$ is the prior distribution of the latent variable z, and $\mathbb{E}_{q_{\phi}(z|\boldsymbol{y})}[\cdot]$ stands for the expected value over the probability distribution $q_{\phi}(z|\boldsymbol{y})$, is approximately equal to finding the Maximum Likelihood estimate. This is due to the fact that

This is because \mathcal{L}_{ELBO} , where ELBO stands for "Evidence Lower Bound", is a lower bound of the data log-likelihood $\log p_{\Lambda}(y)$ (see appendix C).

Kingma and Welling (2013) presented the SGVB estimator for the expected value (in the case where the D_{KL} can not be computed analytically, it can also be estimated) as,

$$\hat{\mathcal{L}}_{ELBO} \approx -D_{KL}(q_{\phi}(z|\boldsymbol{y})||p_{\Lambda}(z)) + \frac{1}{L} \sum_{l=1}^{L} \log(p_{\Lambda}(\boldsymbol{y}|z_{l})), \qquad z_{l} \sim q_{\phi}(z|\boldsymbol{y},\boldsymbol{x}).$$
(26)

If the SGVB framework is used with the a neural networks as the approximate probability distributions $q_{\phi}(z|y)$, then the neural network architecture and minimization scheme is known as Variational Auto-Encoders (Kingma and Welling, 2013), where the model $q_{\phi}(z|y)$ is usually called the "Encoder", and $p_{\Lambda}(y|z)$ the "Decoder".

Sohn et al. (2015) generalized this framework for what they called, Conditional Variational Auto-Encoders (CVAE), where the likelihood and posterior probabilities are allowed to be conditional distributions on a third set of random variables $x \in \mathcal{X}$, $y \sim p_{\Lambda}(y|\mathbf{z},x)$, and $\mathbf{z} \sim q_{\phi}(\mathbf{z}|y,x)$. This is the final configuration we used, but instead of training a generative model as CVAE are usually used to, we used it to solve the inversion problem while simultaneously finding approximate values for the parameters Λ^* , as explained in section Sec. 4.4.1.

450 4.4.1 Stochastic Gradient Variational Bayes framework for approach to solve the Inversion Problem with the SGVB estimator

CVAEs are commonly used to train a generative model $p_{\Lambda}(y|z,x)$ from a probability distribution $p(\mathbf{z}|x)$ that is easy to sample, in order to generate samples that well approximate the target probability distribution (Doersch, 2021). They have been used to

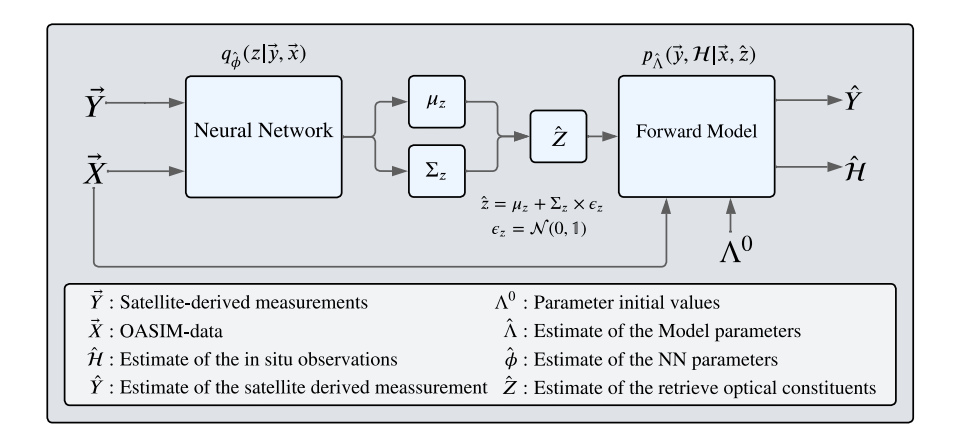


Figure 2. Diagram of the Stochastic Gradient Variational Bayes (SGVB) framework, adapted for the inversion problem, where the estimated \hat{Z} is retrieve retrieved using a parameterized probabilistic function $q_{\phi}(z|\boldsymbol{y},\boldsymbol{x})$, which for our case, is a convolutional feed forward neural network (diagram in Fig. 3) and who's parameters ϕ are learned simultaneously as the parameters Λ , the parameters from the Forward model.

solve inverse problems, like image recovery (Zhong et al., 2019, 2021; Zhao et al., 2023), unfolding in high energy physics (Shmakov et al., 2024), among other applications. In contrast to previous applications of VAEs and CVAEs to inverse methods, in this work, instead of first training a CVAE with latent variables that lack a physical interpretation, we directly used the SGVB framework estimator for the inverse method. Here, $p_{\Lambda}(y|z,x)$ is the likelihood described in Eq. (14), where Λ represents the parameters of the forward function that we aim to optimize, and the latent variable z is the vector that we want to retrieve.

To do so, following the SGVB framework, we used a neural network $q_{\phi}(z|\boldsymbol{y},\boldsymbol{x})$ (diagram shown in Fig. 3) as an approximation of the posterior $p(z|\boldsymbol{y},\boldsymbol{x})$. As described in Kingma and Welling (2013), the \mathcal{L}_{ELBO} is approximated by an empirical expression of the expectation value. The final expression for the loss function is,

$$\mathcal{L}_{ELBO} pprox \sum_{l=1}^{L} \log(p_{\Lambda}(\boldsymbol{y}|z_{l}, \boldsymbol{x})) + D_{KL}(q_{\phi}(z|\boldsymbol{y}, \boldsymbol{x})||p_{\Lambda}(z|\boldsymbol{x})), \qquad \qquad z_{l} \sim q_{\phi}(z|\boldsymbol{y}, \boldsymbol{x}).$$

455

460

465

The expression for $p_{\Lambda}(y|z_l,x)$, used to learn Λ and ϕ , was different from the expression used in section ?? since to train the neural network, all the input data wasscaled between zero and one. Also, we included a term which depends on H^{OBS} to include the in-situ measurements. The final model used was Our model for the Likelihood was,

$$\frac{1}{L} \sum_{l=1}^{L} \log (p_{\Lambda}(\boldsymbol{y}|z_{l})) = \frac{1}{2L} \sum_{l=0}^{L} (\boldsymbol{y}^{d} - \boldsymbol{R}_{rs}^{MODEL}(e^{\tilde{\boldsymbol{z}}^{d}}, \boldsymbol{x}^{d}; \Lambda))^{T} \Sigma_{\epsilon}^{-1} (\boldsymbol{y}^{d} - \boldsymbol{R}_{rs}^{MODEL}(e^{\tilde{\boldsymbol{z}}^{d}}, \boldsymbol{x}^{d}; \Lambda))$$

$$+ (\mathcal{H}^{d}(e^{\tilde{\boldsymbol{z}}^{d}}, \boldsymbol{X}; \Lambda) - H^{OBS, d})^{T} \Sigma_{H}^{-1} (\hat{\mathcal{H}}^{d}(e^{\tilde{\boldsymbol{z}}^{d}}, \boldsymbol{X}; \Lambda) - H^{OBS, d}) \tag{27}$$

where Σ_{ϵ}^{-1} was the equivalent to the covariance matrix introduce in section ??, but transform according to the scaling, Sec. $4.2, \Sigma_H^{-1}$ was chosen in order to have the equivalent to \mathcal{L}^H from Eq. (20), and L is the number of samples used per iteration

, to approximate the expected value. We performed experiments with L=1, L=10, and L=100. The performance of using higher values for L was not significantly higher, for which, we decide decided to use L=10.

The neural network used was We used a neural network composed of two parts, one having as impute output the mean μ_{q_z} , and the other one, the covariance matrix Σ_{q_z} , of a Gaussian probability distribution, in consequence, the DK divergence between two multivariate Gaussian. Since the prior for z is a multivariate Gaussian, the D_{KL} divergence in Eq. 26 is,

$$D_{KL}(q_{\phi}(z|\boldsymbol{y})||p_{\Lambda}(z)) = \frac{1}{2} \left[\frac{|\Sigma_{z}|}{|\Sigma_{q_{z}}|} + \text{Tr}(\Sigma_{q_{z}}^{-1}\Sigma_{z}) + (\mu_{q_{z}} - \mu_{z})^{T} \Sigma_{q_{z}}^{-1} (\mu_{q_{z}} - \mu_{z}) - \dim_{z} \right]$$
(28)

where $|\Sigma_z|$ stands for the determinant of the scaled covariance matrix used for the prior introduced in 4.2, Tr(A) stands for the trace of a matrix A, and dim $_z = 3$, the dimension of z.

Finally, we added a ℓ_2 regularization for the parameters Λ , since it helped for the convergence of the Neural Network. With all the components at hand, the inversion task plus the inference on the parameters is equivalent to approximate the posterior with a parametrized function $q_{\phi}(z|\mathbf{x}, \mathbf{y})$, and find the parameters $\{\phi, \Lambda\}^*$ that minimize the loss function,

480
$$L_{NN} = D_{KL}(q_{\phi}(z|\boldsymbol{y})||p_{\Lambda}(z)) - \frac{1}{L} \sum_{l=1}^{L} \log(p_{\Lambda}(\boldsymbol{y}|z_{l})) - \alpha_{\Lambda}||\Lambda - 1||_{2}$$

$$(29)$$

where $\alpha_{\Lambda}(\Lambda-1)^2$ is the regularization term, with α_{Λ} a hyperparameter tuned as explained in the next section, together with all the other hyperparameters of the method.

4.5 Architecture and Training of the Neural Network

495

As illustrated in Fig. 3, the Neural Network (NN) is composed of three sections, the . The first part has two hidden layers, whose function is to reduce the dimensionality of the input layer by projecting it into the space of the in-situ observations. To achieve it, this part was trained separately from the rest of the NN with in situ observations corresponding to the train data. This preprocessing was done to facilitate the convergence of the final output to values that are physically plausible physically plausible values. The second and third parts are the predicted mean of the latent variable μ_{q_z} and the Cholesky decomposition L_{q_z} square root of the covariance matrix $\Sigma_{q_z} = L_{q_z}^T L_{q_z}$. We choose as output of the NN the Cholesky decomposition, to ensure that the final covariance matrix is positive-defined. In addition, experiments showed that a residual layer at the end of the second part of the NN (adding the first component of the output of the first part), improved the generalization error.

To decide the best hyperparameters of the neural network, we used the library Ray Tune (Liaw et al., 2018), a python Python library designed for parameter tuning, together with the Bayesian Optimization HyperBand algorithm (Falkner et al., 2018) to search in the hyperparameter space. These include the number of hidden layers, the size of the hidden layers, the learning rate, the different moments for the Adam Algorithm used to train the neural network, and the size of the mini-batches.

In the same manner as with the MCMC algorithm, we used the same 90% of the data for training, from which, we select randomly five percent of it as validation for each iteration of the hyperparameter search.

Also, we did an exploration within the activation functions, finding the CELU activation function as the one that returned the best results. The CELU function is similar to the Rectified Linear Unit (ReLU) function, where instead of being the identity

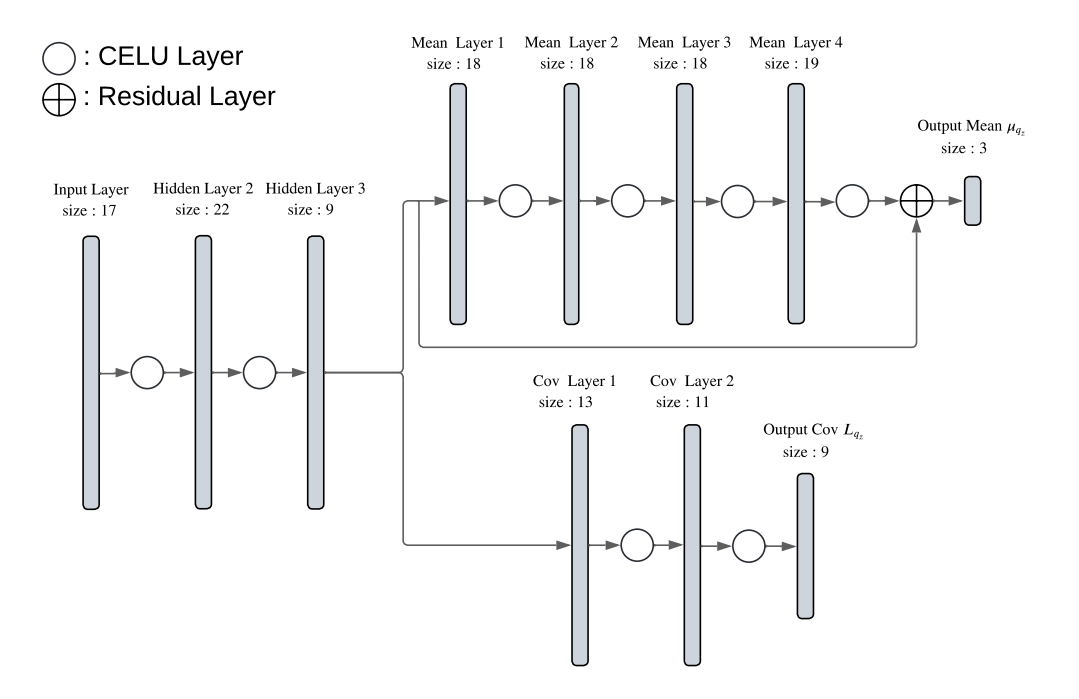


Figure 3. Diagram of the Neural Network (Soto, 2025) used as the parameterized probabilistic function $q_{\phi}(z|z,y)q_{\phi}(z|z,y)$. It is composed of three sections, the first two hidden layers reduce the dimensionality of the input layer by projecting it into the space of the in-situ observations. The output of the second layer is the input of the layers that learn the mean value of the latent variable $\mu_z \mu_{g_z}$, and dose those that learn the Cholezky decomposition L_z components of the square root of the covariance matrix $\Sigma_{g_z} = L_{g_z}^T L_{g_z}$. The dimension of the hidden layers and the number of hidden layers are tuned using Ray Tune (Liaw et al., 2018).

for positive inputs and truncating to zero for negative inputs, it truncates to minus one for negative values and makes a smooth transition between the identity part and the truncation part (Barron, 2017),

$$CELU(x) = \max(0, x) + \min(0, \alpha_c e^{x/\alpha_c} - 1). \tag{30}$$

with With α_c , a hyperparameter also tuned with Ray Tune.

A diagram of the neural network $q_{\phi}(z, y, x) q_{\phi}(z|y, x)$ is presented in Fig. 3, which is part of the framework described in Fig. 505 2. To train the neural network, first the measurements and OASIM-data (X, Y) are passed to it, returning an estimate for the mean and the covariance matrix of the latent variable Z. From these estimates, a random sample is computed, $\hat{Z} = \mu_z + \Sigma_z \epsilon_z$, $\epsilon_z \sim \mathcal{N}(0, \mathcal{I})$, and subsequently used as an estimate in the forward model $\mathbf{R}_{rs}^{MODEL}(e^{\tilde{z}^d}, \mathbf{x}^d; \Lambda)$, and with the observation function $\mathcal{H}(\hat{Z}, \mathbf{X}; \Lambda)$.

5 RESULTS

The results are divided into four parts: the first one focuses on the Bayesian retrieval of the optically active constituents on the surface of the sea and the uncertainty estimation, the second on the parameter optimization, the third part talks about the comparison between the Bayesian outputs and the Variational Bayes approach, and the last one talks about a comparison with a state of the art algorithm for satellite sea surface chlorophyll a estimation.

As described in section

5 5.1 Bayesian Inversion

520

525

We performed the Bayesian inversion from 2005 to 2013. As shown in Fig. 4, the retrieved sea surface chlorophyll manages to reproduce the interannual variability, including the spring algal blooms. The reported uncertainty serves as an estimate of the average expected discrepancy between retrieved data and in-situ measurements, not restricted to chlorophyll observations, but also to the downward light attenuation coefficient and particulate backward scattering coefficient observations. We tested the performance of the inversion with a random sample consisting of 10% of the days with observations. The Root Mean Square Error between the observations and the inverted data was computed (see Tab. D1), as well as the Spearman rank correlation coefficient ρ (Tab. D2), and the relative Median Absolute Deviation rMAD (Tab. D3).

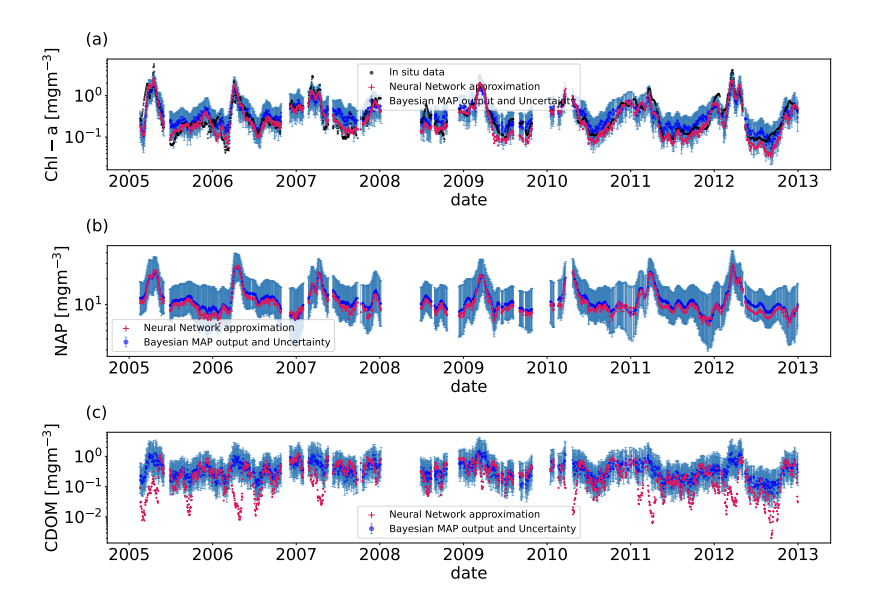


Figure 4. Time series for the chlorophyll- α (a), Non-Algal Particles (b) and Chromophoric Dissolved Organic Matter (c). For all the timelines, the black points are the in-situ observations from the BOUSSOLE buoy, the blue points are the MAP output with uncertainty (blue shadow), using the optimal parameters from the SGVB based framework algorithm, and the red points are the output of the SGVB based framework.

Figure 7 shows a comparison between the true posterior distribution, sampled using the Metropolis-Hasting Algorithm, and the estimated one using the linear approximation, for the inversion of the Remote Sensing Reflectance of February 18, 2005. The true posterior means and standard deviations are closely approximated by the linearization, even if the Forward function

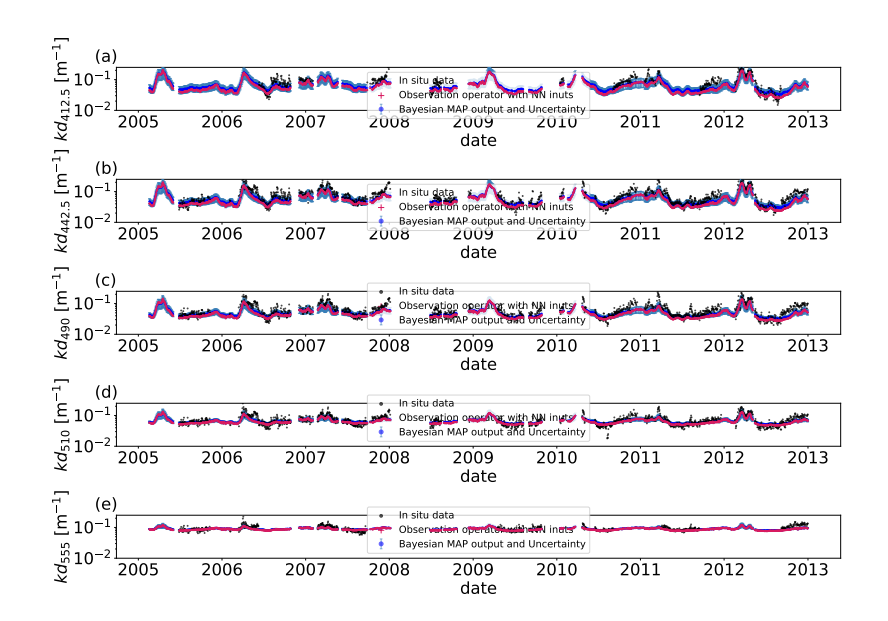


Figure 5. Time series for downward light attenuation coefficient $(k_d(\lambda))$, wavelengths $\lambda = 412.5$ (a), $\lambda = 442.5$ (b), $\lambda = 490$ (c), $\lambda = 510$ (d) and $\lambda = 555$ (e). For all the timelines, the black points are the in-situ observations from the BOUSSOLE buoy, the blue points are the MAP output with uncertainty (blue shadow), using the optimal parameters from the SGVB based framework algorithm, and the red points are the output of the SGVB based framework.

is highly nonlinear. This result is closely related to the choice of the prior $\alpha \mathbb{1} = 1.3\mathbb{1}$ computed as explained in Sec. C, since it is a strongly informative prior. We can study the effect of the prior by computing the inverse of the Fisher information matrix, since the Cramér–Rao bound states that the variance of the MLE is always higher than or equal to this quantity:

$$\operatorname{Var}[\hat{\psi}] \ge \frac{1}{\operatorname{I}(\psi)} \tag{31}$$

where $\hat{\psi}$ is an unbias estimator of a random parameter ψ , and $I(\psi)$ is the Fisher information matrix, defined as

$$I(\psi) = -\mathbb{E}\left[\frac{d^2\mathcal{L}(X;\psi)}{d\psi^2}\right]$$
(32)

where $\mathcal{L}(X;\psi)$ is the likelihood of a random variable X with parameters ψ (Cramér, 1999). For our case, the Fisher information matrix is equal to

$$I(\Lambda) = \mathbf{K}^T \Sigma_{\epsilon}^{-1} \mathbf{K} \tag{33}$$

which is equal to the inverse of Eq. 19 without the effect of the prior. To quantify the effect of the prior, we divided the average Frobenius norm of the inverse of the Fisher information matrix $||1/I(\Lambda)||_{2,2}$ and the retrieved covariance matrix $||\Sigma_{\bar{z}d}||_{2,2}$, obtaining the value of 42.9, which means that the prior is reducing the uncertainty of the MLE by a factor of 42. On the other

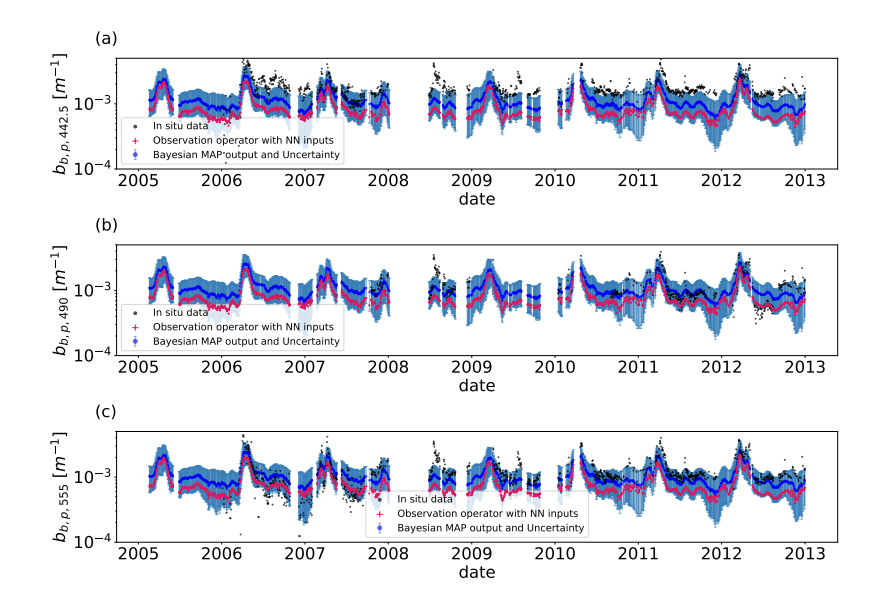


Figure 6. Time series for particulate backward scattering coefficient for the wavelengths $\lambda = 442.5$ (a), $\lambda = 490$ (b) and $\lambda = 555$ (c). For all the timelines, the black points are the in-situ observations from the BOUSSOLE buoy, the blue points are the MAP output with uncertainty (blue shadow), using the optimal parameters from the SGVB based framework algorithm, and the red points are the output of the SGVB based framework.

hand, this highly informative prior is a reasonable prior, since it states that most of the chlorophyll concentration should be within values lower than $\exp(\mu_z + 2\sigma_{\bar{z}}) = \exp(2.6) = 13.46 \text{mgm}^{-3}$ and higher than $\exp(\mu_z - 2\sigma_{\bar{z}}) = \exp(-2.6) = 0.07 \text{mgm}^{-3}$.

5.2 Optimization of the forward model parameters

540

545

550

As described in Sec. 4.3.1, we tuned twenty-six twenty-four parameters, multiplying them by fourteen perturbation factors, to minimize the distance between retrieved quantities and observation data. We are interested in the optimized parameter values, as well as the uncertainties. If any of our final parameterizations are going to be used in future works, it is important to note that we are finding optimal parameters that are representative of data from different seasons. For this reason, we present a sensitivity analysis, where we can appreciate the annual variability of the sensitivity. Parameters with high variability may need special considerations for models that use different parameterizations for different seasons.

Following Carmichael et al. (1997), the sensitivity of the Remote Sensing Reflectances, downward light attenuation coefficient and backward scattering coefficient can be computed by calculating the partial derivative with respect of the different parameters $(\partial R_{RS}/\partial \delta_i, \partial kd/\partial \delta_i, \partial b_{b,p}/\partial \delta_i)$, named the local sensitivity coefficients, and normalized with respect to the sensitivity coefficient $(R_{RS}/\delta_i, kd/\delta_i, b_{b,p}/\delta_i)$ to obtained dimensional adimensional quantities. The results can be observed in Fig. 8.

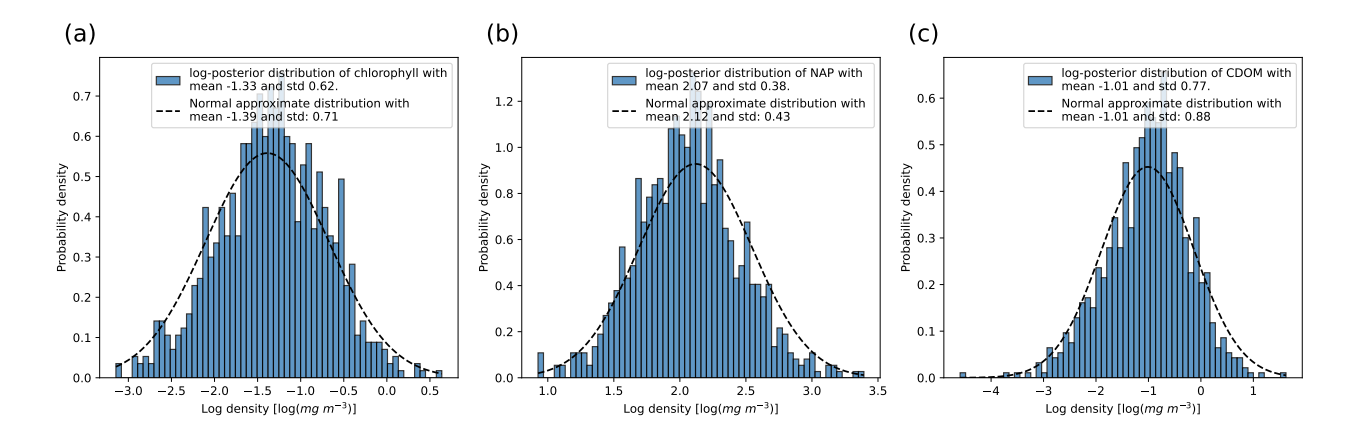


Figure 7. Comparison between the true posterior distribution (Eq. 16) and the approximate posterior by following the algorithm in Algorithm 1 for the log-posterior distribution of (a) chlorophyll- α , (b) Non Algal particles and (c) Colored Dissolved Organic Matter, for the first day of the train data (February 18, 2005). The true posterior (in blue) was sampled using the Metropolis-Hasting Algorithm (see Algorithm 2), while the normal approximation (dashed line) was derived by linearization of the forward model around the MAP estimate.

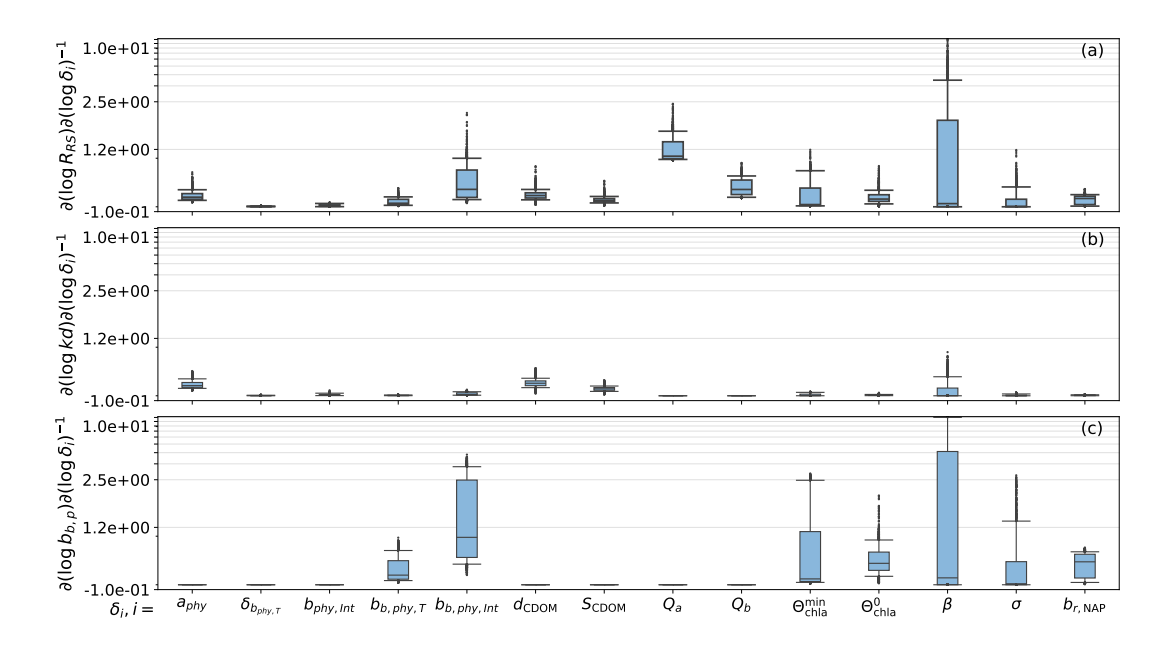


Figure 8. Sensitivity of (a) R_{rs} , (b) kd and (c) $b_{b,p}$ with respect to the perturbation factors δ_i evaluated at $\delta_i = 1$, the box plots represent the quartiles of the sensitivity for each day.

We noticed that R_{RS} and $b_{b,p}$ share a strong variability in the sensitivity with respect to the backward scattering coefficient of phytoplankton $b_{b,phy}$ and Non Algal Particles $b_{b,NAP}$ $b_{b,phy}$ and backscattering-to-scattering ratio of NAP, $b_{r,NAP}$, as well as the parameters $\Theta_{\text{chla}}^{\min}$, Θ_{chla}^{0} , β , σ , which form part of the $\frac{chla}{chla}$: C-chla: C ratio relation described in Eq. (3). This agrees with

555

the seasonal variability in the abundance of the different phytoplankton functional types (Lazzari et al., 2012), as well as the variability in concentrations of pollution (Bodin et al., 2004). With this observation, we expect that using only one set of parameters for the full year would result in suboptimal predictions. Nevertheless, we proceed to find the optimal parameters that described the full historical data set.

To do so, we performed a an MCMC algorithm as described in section Sec. 4.3.1. An example of the distribution obtained for each parameter can be observed in Fig. 9. The original values as well as the mean and standard deviation for the λ -dependent parameters can be appreciated in Fig. 10. Finally, the original values as well as the statistics obtained using the MCMC algorithm for the λ -independent parameters can be appreciated in Table Tab. 4.

560

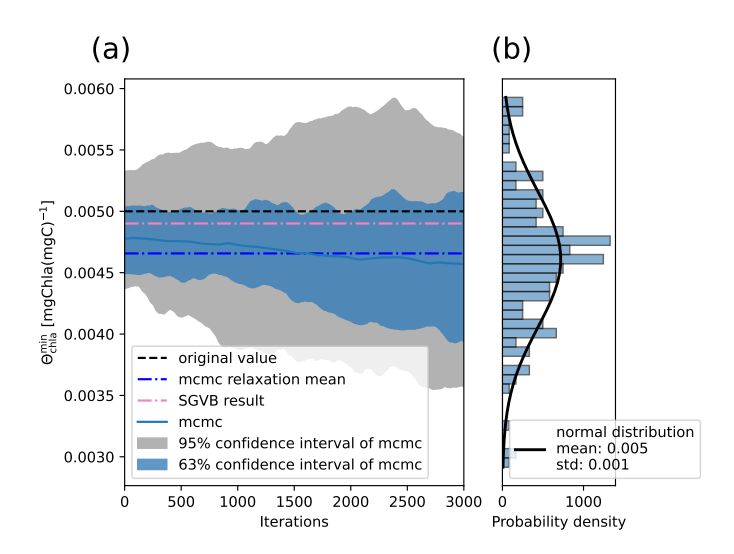


Figure 9. Result of the Metropolis-Hasting Algorithm for the parameter $Q_bQ_{chla}^{min}$ [mgChla(mgC)⁻¹], using the transition probability shown in Eq. (23), with initial conditions close to the value obtained after performing Alternate Minimization. (a) Evolution of the parameter after each iteration of the algorithm, (b) final probability density estimated as a Gaussian distribution.

In order to assess the normality of the final distributions, we performed a Kolmogorov-Smirnov test. Using a threshold value of 0.05, we arrived to the conclusion that most of the parameters agree with the hypotheses that they follow a Gaussian distribution, with the exception of β , and S_{CDOM} . For this reason, except the parameters just mentioned, we can use the standard deviation as a measure of the uncertainty. For β and, S_{CDOM} we reported the standard deviation as uncertainty, remarking that the final result didn't agree with the hypothesis that they followed a Gaussian distribution.

We For completeness, we also computed the covariance matrix between the perturbation factors δ_i , which can be appreciated in table 5. We observed a strong correlation between d_{CDOM} , S_{CDOM} , Q_a and Q_b . The correlation between the former two is evident by observing Eq. (4), and the latter ones in Eq. (8), but the correlation between them is not trivial. Tab. 5.

As an alternative method, we compared the results obtained by using the SGVB framework with those obtained with the MCMC algorithm and the MAP estimates of the optical constituents z. The final parameters obtained can also The main result of the new parametrization is a decrease in the Root Mean Square Error RMSE between the test data of sea surface chlorophyll

Table 4. Original values, final values obtained using the SGVB frameworkestimator, as well as the mean, standard deviation and Kolmogorov-Smirnov test coefficient for the sampling with the Metropolis-Hasting Algorithm for the λ -independent parameters.

	Original value	CVAE-SGVB	MCMC result	KS test for normality	KS p-value for normality
		result			
d_{CDOM} d_{CDOM}	0.0150	0.0151	0.0146 0.0101 ±	0.05240.0536	0.7525 7,259E-01
$[\frac{\text{m}^2(\text{mgCDOM})^{-1}}{\text{m}^2(\text{mgC})}]$	~~~~	0.0156	0.00200.0028	100000	1000000
Schom Schom [nm]	0.0170	0.0163	0.0122 <u>0.0099</u> ±	0.11140.0553	0.0348 6.907E-01
		0.0111	0.00200.0005		
Q_a	5.3300	5.9301	5.3145 5.3861 ±	0.05520.0495	0.6932 8.087E-01
		4.4960	0.4657 0.2899	100000	
Q_b	0.4500	~~~~	~~~~		
•		0.4265	0.4459 <u>0.4441</u> ±	0.08690.0742	0.1683 3.250E-01
		0.4283	0.03140.0463		
	0.0050				
$\Theta_{\text{chla}}^{\min}$ $\Theta_{\text{chla}}^{\min}$		0.0050	0.0058 <u>0.0048</u> ±	0.0755 0.0708	0.3053 3.810E-01
$[\frac{\text{mgChla}(\text{mgC})^{-1}}{\text{mgChla}(\text{rg})}]$	ngC	0.0049	0.0005 0.0006		
Θ_{chla}^0 Θ_{chla}^0	0.0300	0.0298	0.0301 0.0296 ±	0.06960.0637	0.4019 5.135E-01
[mgChla(mgC) ⁻¹ mgChla(r	$mgC)^{-1}$]	0.0251	0.00240.0027		
β	500.0000	,,,,,,,,,,,,,,,,,,,,,,,,,,,,,,,,,,,,,,,	700000		
[mmolm ⁻² s ⁻¹ mmolm ⁻² s ⁻	·1 ₁	616.2043	536.1500 <u>558.5273</u> ±	0.13870.1090	0.0038 4.129E-02
	~	589.2924	35.3500 33.5500		
σ	20.0000				
$[\frac{\text{mmolm}^{-2}\text{s}^{-1}}{\text{mmolm}^{-2}\text{s}^{-1}}]$	·1]	19.9735	24.3895 <u>18.8886</u> ±	0.09270.0732	0.1203 3.420E-01
		20.3714	1.8762 2.2417		
$b_{b, ext{NAP}}b_{r, ext{NAP}}$	0.0050	0.0045	0.0052 0.0041 ±	0.08220.0545	0.2180 7.077E-01
		0.0024	0.00050.0008		

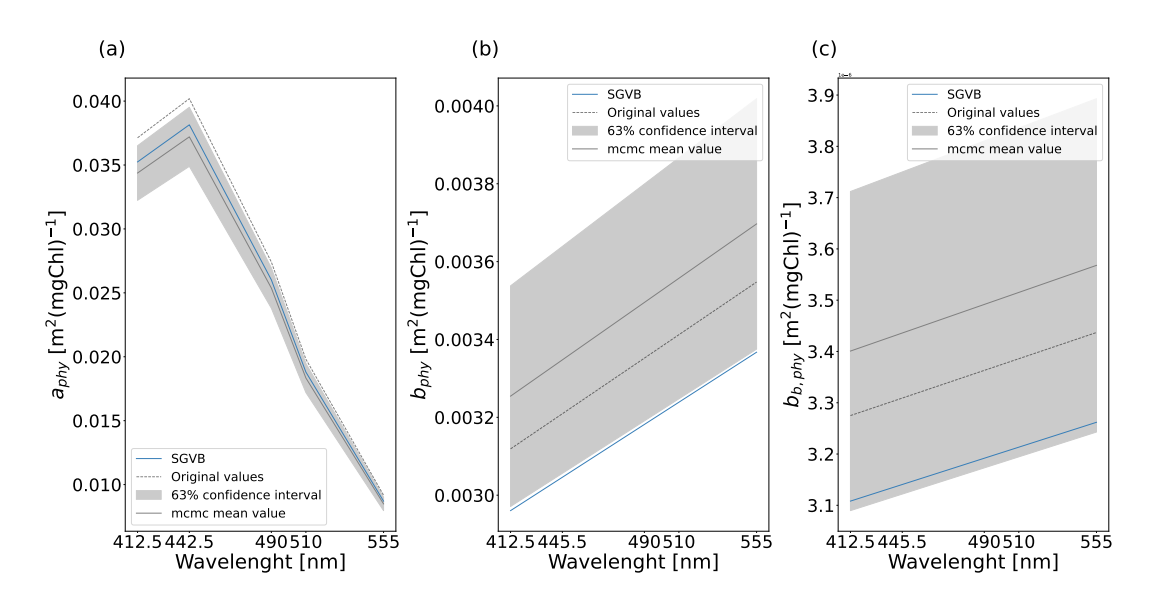


Figure 10. Original values (dashed line), final values using the SGVB based framework (blue) as well as the mean and standard deviation (gray) for the λ -dependent parameters (a) absorption coefficient of phytoplankton $a_{phy}(\lambda)$, (b) scattering coefficient of phytoplankton $b_{phy}(\lambda)$ and (c) backward scattering coefficient of phytoplankton $b_{b,phy}(\lambda)$.

Table 5. Correlation matrix between the perturbation factors δ_i , computed using the samples from the Metropolis-Hasting Algorithm.

$\delta_i, i =$	a_{PH}	$b_{ extstyle $	$b_{ exttt{phy,Int}}b_{ exttt{phy,Int}}$	$b_{b,\mathrm{phy},T}$	$b_{b, ext{phy,Int}}b_{b, ext{phy,Int}}$	d_{CDOM} d_{CDOM}	$S_{\text{CDOM}}S_{\text{CDOM}}$	Q
$a_{ extstyle phy} a_{PH}$	1.00							
$b_{\mathrm{phy},T}$	0.15-0.04	1.00						
$b_{ m phy,Int}$ $b_{ m phy,Int}$	-0.16 <u>0.17</u>	-0.01_0.12	1.00					
$b_{b,\mathrm{phy},T}$	0.05	0.21 - 0.01	-0.09 - <u>-0.01</u>	1.00				
$b_{b, ext{phy,Int}}b_{b, ext{phy,Int}}$	-0.06 0.06	0.15-0.08	0.39 -0.07	0.07 0.09	1.00			
$\frac{d_{ ext{CDOM}}}{d_{ ext{CDOM}}}$	0.21_0.47	0.23 -0.05	0.22_0.02	-0.02 -0.04	0.43 0.03	1.00		
S_{CDOM} S_{CDOM}	0.24 0.19	0.31-0.09	0.24_0.08	-0.19 -0.04	0.38 -0.05	0.73 <u>0.61</u>	1.00	
Q_a	0.23 -0.52	0.28 0.10	0.24 -0.04	-0.15 -0.02	0.22 -0.03	0.410.05	0.62 0.38	1.0
Q_b	-0.11- 0.28	0.25 -0.10	-0.08	-0.01	0.32-0.08	-0.03 - <u>0.06</u>	0.02-0.16	-0.02
$\Theta_{\mathrm{chla}}^{\mathrm{min}}$ $\Theta_{\mathrm{chla}}^{\mathrm{min}}$	$\underbrace{0.08}_{\textstyle \bullet} \underbrace{0.02}_{\textstyle \bullet}$	0.11 - <u>-0.02</u>	-0.09 <u>0.07</u>	<u>-0.11</u>	0.13	-0.12 <u>0.11</u>	-0.08 -0.04	-0.18
$\Theta_{ ext{chla}}^0 \! \! \! \! \! \! \! \! \! \! \! \! \! \! \! \! \! \! \!$	0.06-0.07	-0.01 0.25	0.02_0.08	0.10	0.08 - <u>-0.07</u>	-0.17 <u>0.05</u>	-0.10 0.08	-0.10
β	-0.13-0.44	-0.21 0.23	-0.13 0.23	0.22 0.28	-0.21- 0.16	-0.50 - <u>0.30</u>	-0.73 <u>-0.32</u>	-0.49
σ	-0.03 <u>-0.02</u>	-0.15 -0.07	0.25_0.23	0.15-0.16	0.14 - 0.05	-0.04 -0.02	-0.16 <u>-0.20</u>	0.01_(
$b_{b, ext{NAP}}$ $b_{ ext{r}, ext{NAP}}$	0.00-0.24	-0.11 0.13	-0.10 -0.00	-0.20 -0.19	-0.09 - <u>0.04</u>	0.04-0.42	0.07- 0.41	-0.03

observations and inverted values. A key aspect to note is that the MLE computed using the train data can present overfitting; for this reason, we had to use early stopping during the Alternate Minimization step, and then we proceeded to use the mean value

of the estimated posterior estimated with the MCMC samples. Since for the test data, we observed a decrease in the RMSE (see Tab. D1), we can say that the posterior mean is good for generalization.

5.3 Comparison between Bayesian retrievals and the Variational Bayes approach

590

595

600

605

610

As described in Sec. 4.4, we used the SGVB estimator to find an optimal parametrization. The results can be appreciated in table Tab. 4 and Fig. 10. Taking into account the uncertainty of the MCMC results, and using the 95% confidence interval, we see that only the parameters 22 of the 24 parameters perturbed with the SGVB estimator agree with the MCMC estimation, in the sense that the SGVB output is within the uncertainty of the MCMC estimate. The two parameters with high discrepancy between the two frameworks are: Q_a , Q_b , Θ_{chla}^{min} , Θ_{chla}^0 and $b_{b,NAP}$ agree in the final values. Nevertheless, in order to assess the ability of the resulting parameters optimize the forward model, we computed the MAP estimate of the latent variable in average, the most sensitive parameter concerning Remote Sensing Reflectance, and $b_{\tau,NAP}$, one of the most sensitive parameters concerning particulate backward scattering.

To assess the performance of each set of parameters, we evaluated the MAP estimates of the optical constituents z for the test set of the historical data, a set of data that given each set of parameters (MAP estimate obtained with the MCMC algorithm and the MLE obtained with the SGVB estimator) for the test dataset. I recall that this data set was not used for training of the neural network in any way, or to estimate the parameters in any any parameter tuning before, so these results serve as a confirmation of the robustness of the methods.

These estimates were computed with the original values of the parameters, for the mean values obtained with the MCMC algorithm and with the parameters obtained with the SGVB framework. The result is that in terms of The main indicator will be the sea surface chlorophyll observations, as it is the least noisy and scattered observation data. Based on the Root Mean Square Error (RMSE) and relative Median Absolute Deviation (rMAD) between measurements and MAP estimates, values that can be appreciated in table D1, both methods optimized the forward model, and for some measurements, including the in-situ observations of chlorophyll, retrieved estimates (Tab. D1 and Tab. D3), both parameter sets improved the inversion results. However, the parameters obtained with the SGVB framework outperform the MCMC results. The disparity between the parameters means that parameter set optimized using the SGVB estimator yielded the best performance.

The observations of the downward light attenuation coefficient and the particulate backward scattering coefficient are much more scattered and noisy than the chlorophyll, yet the SGVB parameters optimized all the model output matching observations, while the MCMC favors better outputs only for the k_d values. We speculate that this is due to overfitting as the measurements of particulate backward scattering are highly scattered, and as particulate backward scattering is sensitive to $b_{r,NAP}$, the posterior probabilities that we are attempting to maximize are multi-modal, with the Alternate Minimization in combination with the MCMC algorithm finding one set of optimal parameters, while the SGVB framework finding a different oneestimated value from the MCMC could be bias for the noise. In the case of NN training we used minibatch minimization, this may have helped to find a parameter value that is better for generalization.

The SGVB framework estimator also provides an efficient way of computing estimates of the optical constituents z, which, by construction, are also consistent with the forward model, and present equivalent values for the with optimal RMSE between

measurements and estimates. Since they are computed with a neural network, the computational time outperforms the standard implicit inversion methods, required in cases where the expression of the RTE is too complicated to invert it analytically. For completeness, in tables D2 and D3, we also present the Pearson correlation coefficients and the relative Median absolute deviation (rMAD) between measurements and estimates comparison, the estimated optical constituents \hat{z} using the SGVB estimator are shown in Fig. 4, Fig. 5 and Fig. 6, and the timelines for the values estimated in Fig. 4, 5 and 6. statistics for the observation operator using these estimates are shown in Tab. D1, Tab. D3 and Tab. D2.

This timelines illustrates the ability of the inverse methods to describe the seasonal variability. We also notice that the uncertainty increase for days when the discrepancy between measurement and prediction is bigger, reaffirming the advantages of including uncertainty in We observe that the standard Bayesian estimate and those using the SGVB estimator are close to each other (Fig. 4), since the SGVB estimator outputs are within the uncertainty of the Bayesian estimate. Differences between both could be due to model errors, since the SGVB estimator requires approximating the posterior with a parameterized probability distribution, in our case, a Neural Network, or differences between the training algorithms. The Variational Bayes method also estimates the covariance matrix between the latent variables Z, nevertheless, since the uncertainty was underestimated, we only plotted the mean values.

5.4 Comparison with satellite products

615

620

625

630

To asses the validity of the results with respect of state of the art algorithms, we compared the capability of the DIIM system in a wider region in the North West Mediterranean Sea characterized by high dynamics regimes of vertical mixing during the spring period and stratification during summer. The comparison is carried out using additional in-situ data (not used in the calibration of DIIM) based on High-Performance Liquid Chromatography (HPLC, Di Biagio et al., 2025) and a standard Ocean Color retrieval approach used with Copernicus Marine Service, the predictions. For the derived quantities $kd(\lambda)$ and $b_{b_p}(\lambda)$, for some cases, the standard error propagation method under-estimated the uncertainty, especially for $kd(\lambda)$ with λ greater than MedOC4.2020 (Colella et al., 2025). The latter approach is based on a calibrated nonlinear regression of the maximum Rrs in the wavelengths at 443, 490, and 510 nm-, normalized over Rrs at 555 nm;

chlorophyll_{satellite} =
$$10^{(a_0 + a_1 X + a_2 X^2 + a_3 X^3 + a_4 X^4)}$$
, $X = \log_{10} \left(\frac{\max(R_{rs,443}, R_{rs,490}, R_{rs,510})}{R_{rs,555}} \right)$

$$a_0 = 0.327, a_1 = -2.994, a_2 = 2.722, a_3 = -1.226, a_4 = -0.568. \tag{34}$$

Nevertheless, the values of R_{RS} computed with the estimated optical constituents are consistent with the satellite observations for all the wavelengths computed, as can be confirmed with To do so, we computed the values of RMSE in table D1, rMAD in table D3 and correlation in table D2. surface downward direct and scattered irradiance as described in Lazzari et al. (2020) for the days and places where in-situ measurements were taken (see Fig. 11, (A)). We chose a square of $4^{\circ} \times 4^{\circ}$ close to the BOUSSOLE buoy for the samples, and selected those with a bathymetry lower than 200 m, and samples performed at less than 10 meters deep. For the Remote Sensing Reflectance (CMEMS), we used an average of 5 days, \sim 5 km window

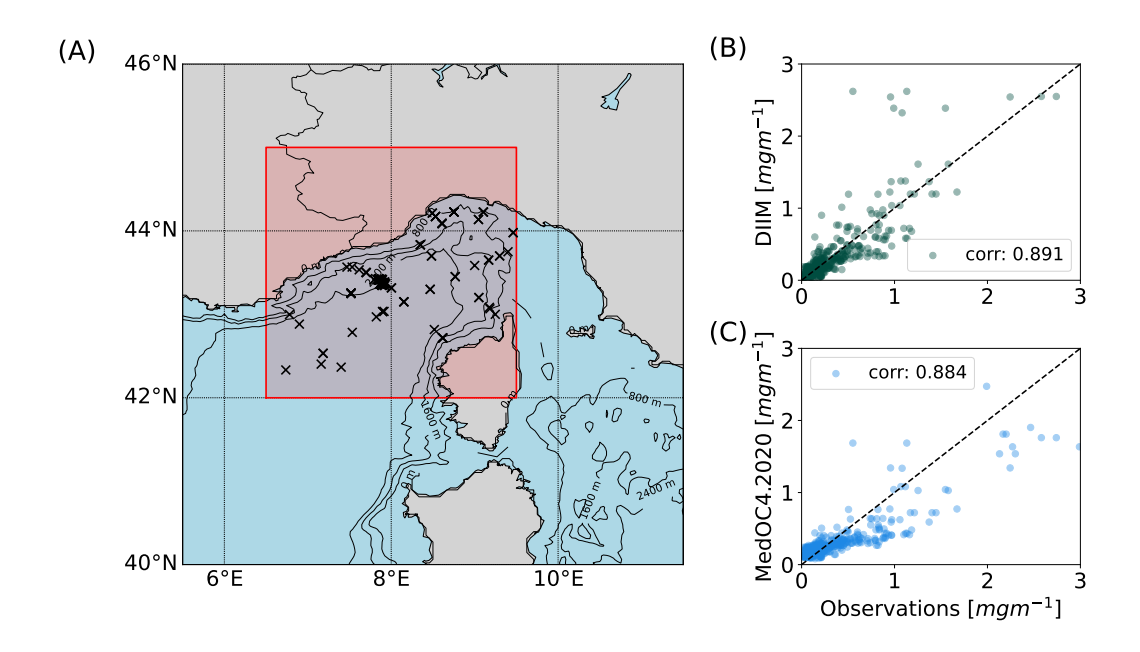


Figure 11. (A) Region in red and place with in-situ measurements (x) for the comparison between (B) the inverted values of chlorophyll a using the SGVB estimator, and (C) a standard Ocean Color retrieval approach used with Copernicus Marine Service (Colella et al., 2025).

around the points. Finally, we used the SGVB estimator to invert the Remote Sensing Reflectance and estimate the Chlorophyll concentration. The outputs can be observed in Fig. 11.

Results are consistent between in-situ data and inversion models, suggesting that the present approach is applicable over spatially heterogeneous conditions.

645 6 Discussion

650

655

In the last years, there has been an increasing number of applications of neural networks in earth sciences, like forecasts of the El Niño-Southern Oscillation (ENSO) by using historical simulations and a convolutional neural network (Ham et al., 2019), fusion of satellite data (Chapman and Charantonis, 2017; Denvil-Sommer et al., 2019; Bocquet et al., 2020), classification of regions on the ocean (Richardson et al., 2003; Saraceno et al., 2006), finding drivers of net primary productivity using self organizing maps (Lachkar and Gruber, 2012), reconstruction of oceanographic variables (Martinez et al., 2020; Pietropolli et al., 2022), classification of the anomalies of water leaving radiance (Mustapha et al., 2014), data reconstruction (Manucharyan et al., 2021; George et al., 2021), inversion of oceanographic variables (Brajard et al., 2006; Irrgang et al., 2019; Dessailly, 2012), pattern recognition (Maze et al., 2017; Jones et al., 2019; Jones and Ito, 2019; Boehme and Rosso, 2021; Desbruyères et al., 2021), forecast imposing physical constrains (De Bézenac et al., 2019; Erichson et al., 2019), increase of the resolution of modeling (Barthélémy et al., 2022), among others.

Our work makes use of a neural network to approximate the posterior probability distribution of optical constituents in the sea by employing the SGVB frameworkestimator. As described in section Sec. 4.4.1, we minimized maximise the ELBO loss function, which simultaneously optimized optimizes the forward model by finding the MLE of the parameters, deriving in-situ in situ biogeochemical parameters for reflectance observations, linking the neural network procedure to an interpretable model. The novelty of our approach is the implicit inclusion of the model uncertainty in the results. In fact, the output approximates the true MAP estimate given a set of measurements. As stated by Kingma and Welling (2013), this approach is especially useful to do inference of intractable posteriors and to find the MLE of the forward model parameters, a situation commonly encountered in data assimilation problems, where the number of parameters to optimize makes the problem intractable. This work serves as a test bed, comparing the more traditional Bayesian Inference approach with the results obtained with the SGVB estimator, as well as presenting a pointwise observation operator for the active optical constituents chlorophyll, NAP and CDOM.

660

670

675

680

685

690

On the other hand, our Our results with the SGVB framework estimator under-estimated the uncertainty of the optical constituents, a-computation that is of crucial importance for multiple applications, like objective comparison of simulations against observations, efficient assimilation of data with methods like the Kalman Filters, among others (Brankart et al., 2012). The A further analysis of the effect that each term of the loss function has on the NN covariance matrix would be needed, as well as whether the inclusion of a regularization term is affecting the uncertainty estimation. For the moment, the requirement of reliable uncertainty estimations lead-leads us to use only the point-ways estimate of the neural network. Furthermore, we explored the Bayesian approach, approximating the final posterior distribution of the optical constituents, $p_{\Lambda}(z|y,x)$, with a Gaussian probability distribution. This method returns estimates with reliable uncertainty estimations that can be used in real operational systems.

In particular, in addition to the optical constituents, our aim was we aimed to find the optimal model with respect to all the in-situ observations for the entire time spanperiod. This ambitious goal made the final results suboptimal for some individual measurements. For example, Salama and Verhoef (2015) used a similar forward model with the aim of estimating the to estimate the downward light attenuation coefficient at a wave-length wavelength of 490 nm, kd(490), at different depths, obtaining a rMAD of 11.84%, while our result using the MCMC parameters presented a rMAD value of 2221%. We noticed that by optimizing only one in-situ measurement, we could find a set of parameters that made that measurement more precise. Nevertheless, we decided to use the parameters presented —to balance the global accuracy. For example, in terms of the rMAD of the Remote Sensing Reflectance at a wavelength of 490 nm, $R_{rs}(490)$, we obtained a value of rMAD of 1.21.8%, outperforming previous works.

Our approach also differs from other works on Bayesian estimation of optical constituents (Gordon and Boynton, 1997; Boynton and Gordon, 2000; Michalopoulou et al., 2009; Erickson et al., 2023), since we are employing a three steam model, derived from the Radiative Transfer Model (Dutkiewicz et al., 2015), and using it to derived the in-situ observations for all the wave-lengths available. This feature allows scientists to understand the automatic learning process in terms of meaningful physical parameters.

The approach can be extended in different directions, in particular, the addition of more optical constituents, which will be facilitated once the information of the new satellite missions PRISMA (Hyperspectral Precursor of the Application Mission),

with 12 nm spectra resolution ranging from 400 to 2500 nm, and PACE (Plankton, Aerosol, Cloud, Ocean Ecosystem) with a 5 nm resolution ranging from 350 to 890 nm, is used as input of the system, or the addition in the Forward model of terms that take into account the interaction with the sea floor, crucial for the analysis of shallow waters.

7 CONCLUSIONS

705

By utilizing the Bayes theorem and linearizing the forward function, we achieved the inversion of the optical constituents, with an estimate of the uncertainty. The latter is fundamental for the assimilation of Remote Sensing Reflectance.

By using an MCMC algorithm, we computed a set of parameters that optimized the forward model —and showed that the solution was not unique by using the SGVB frameworkmethod was robust by obtaining coherent values with the SGVB estimator. Moreover, the SGVB—Variational Bayes framework can be used as an alternative to find point-wise estimates of optimal parameters, and also as an efficient way of computing point-wise estimates of the optical constituents.

Regarding the computational advantages of the SGVB frameworkestimator, as long as the uncertainty is not required, it is the best option to estimate the optical constituents in operational systems, since, after training, the evaluation of the neural network is much faster than the iterative minimization (effect known as amortization). Nevertheless, the posterior probability learned by the neural network under-estimated underestimates the uncertainty of the result, which makes the MAP algorithm preferred when the uncertainty is a requirement. Since the computational time for the MAP estimate depends from on the initial conditions, we proposed to use the SGVB estimates as initial conditions for the MAP algorithm, which, by making experiments with our current implementation, we found that is capable to reduce to be capable of reducing the number of steps by more than 50%.

For future work, it would be important to apply and verify the accuracy of the approach with more optical constituents and to test Remote Sensing Reflectance assimilation in a biogeochemical model.

Code and data availability. The version used to produce the results is archived on Zenodo, as are the input data and scripts to run the model and produce the plots for all the simulations presented in this paper, under the DOI 10.5281/zenodo.14609747 (Soto, 2025).

We used the MedBGCins data set for in-situ data based on High-Performance Liquid Chromatography. Data set available in Zenodo under the DOI https://doi.org/10.5281/zenodo.15489967 (Di Biagio et al., 2025).

715 Appendix A

In this section, we expand the solution of Eq. (1) subject to the boundary conditions (6), under the homogeneity assumption. First, for simplicity, we re-write Eq. (1) as,

$$\begin{split} \frac{dE_{\rm dir}(h,\lambda)}{dh} &= -c_d(\lambda)E_{\rm dir}(h,\lambda),\\ \frac{dE_{\rm dif}(h,\lambda)}{dh} &= -C_s(\lambda)E_{\rm dif}(h,\lambda) + B_u(\lambda)E_u(h,\lambda) + F_d(\lambda)E_{\rm dir}(h,\lambda),\\ \frac{dE_{\rm u}(h,\lambda)}{dh} &= -B_s(\lambda)E_{\rm dif}(h,\lambda) + C_u(\lambda)E_u(h,\lambda) - B_d(\lambda)E_{\rm dir}(h,\lambda), \end{split}$$

subject to,

$$E_{\rm dir}(0,\lambda) = E_{\rm dir}^{\rm OASIM}(0,\lambda), E_{\rm dif}(0,\lambda) = E_{\rm dif}^{\rm OASIM}(0,\lambda), E_{\rm u}(\infty,\lambda) = 0, \tag{A1}$$

were,

$$c_{d}(\lambda) = \frac{a(\lambda) + b(\lambda)}{\cos \theta},$$

$$C_{s}(\lambda) = \frac{a(\lambda) + r_{s}b_{b}(\lambda)}{v_{s}},$$

$$B_{u}(\lambda) = \frac{r_{u}b_{b}(\lambda)}{v_{u}},$$

$$F_{d}(\lambda) = \frac{b(\lambda) - r_{d}b_{b}(\lambda)}{\cos \theta},$$

$$B_{s}(\lambda) = \frac{r_{s}b_{b}(\lambda)}{v_{s}},$$

$$C_{u}(\lambda) = \frac{a(\lambda) + r_{u}b_{b}(\lambda)}{v_{u}},$$

$$B_{d}(\lambda) = \frac{r_{d}b_{b}(\lambda)}{\cos \theta}.$$
(A2)

Equation (A1) is a linear system of Ordinary Differential Equations, which can be solved by, first solving the equation for $E_{\text{dir}}(h,\lambda)$, followed by solving the system of equations for $E_{\text{dir}}(h,\lambda)$ and $E_{\text{u}}(h,\lambda)$, taking the solution of $E_{\text{dir}}(h,\lambda)$ as the in-homogeneous part of the system of equations. The final expression expression is,

$$E_{\text{dir}}(h,\lambda) = E_{\text{dir}}^{\text{OASIM}}(0,\lambda)e^{-hc_d},$$

$$E_{\text{dif}}(h,\lambda) = c^+e^{-k^+h} + x_{\text{dif}}E_{\text{dir}}(h,\lambda),$$

$$E_u(h,\lambda) = c^+r^+e^{-k^+h} + y_uE_{\text{dir}}(h,\lambda),$$
(A3)

725 where,

$$c^{+} = E_{\text{dif}}^{\text{OASIM}}(0,\lambda) - xE_{\text{dir}}^{\text{OASIM}}(0,\lambda),$$

$$k^{+} = D - C_{u},$$

$$r^{+} = \frac{B_{s}}{D},$$

$$D = \frac{1}{2} \left(C_{s} + C_{u} + \sqrt{(C_{s} + C_{u})^{2} - 4B_{s}B_{u}} \right),$$

$$x = \frac{(-(C_{u} + c_{d})F_{d} - B_{u}B_{d})}{(c_{d} - C_{s})(c_{d} + C_{u}) + B_{s}B_{u}},$$

$$y = \frac{(-B_{s}F_{d} + (-C_{s} + c_{d})B_{d})}{(c_{d} - C_{s})(c_{d} + C_{u}) + B_{s}B_{u}}.$$
(A4)

For completes, in In the case when the expression $(c_d - C_s)(c_d + C_u) + B_s B_u = 0$, then the expression for c^+ has to be exchange to $c^+ = E_{\rm dif}^{\rm OASIM}(0,\lambda)$.

Appendix B: Tuning of the hyperparameter α

As seen in section Sec. 4, the final covariance matrix for the retrieve \tilde{Z}^* depends on the hyperparameter α thought Σ_z by the equation $\Sigma_z = \alpha 1$. We selected the value of α to fulfill two criteria, the final result for: The retrieved \tilde{Z}^* should not depend be robust on α , meaning, small changes on α should not change the retrieved quantity, and the estimated uncertainty has to be close to the discrepancy between retrieved data and in-situ observations.

For this end, we defined the error of the forward model $\epsilon_{R_{rs}}(\alpha)$ as the Root Mean Square Difference between the satellite Remote Sensing Reflectance and the that predicted by the model. We expect this quantity to not depend. The aim is to make this quantity robust on α .

We also defined the error between the predicted uncertainty and the actual discrepancy between model and data $\epsilon_{\delta_{\text{chla}}}(\alpha)$, where the predicted uncertainty is estimated as the mean value of the standard deviation of the predicted chla^{MODEL}, and the discrepancy between model and data is estimated as the Root Mean Square Difference between chla^{OBS} and chla^{MODEL}.

740 We selected the parameter α that minimized this two errors.

We-computed $\epsilon_{R_{rs}}(\alpha)$ and $\epsilon_{\delta_{\text{chla}}}(\alpha)$ for different values of α until the curve $\epsilon_{R_{rs}}(\alpha)$ flattens. With the errors computed, we re-scaled the error functions $\epsilon_{R_{rs}}(\alpha)$ and $\epsilon_{\delta_{\text{chla}}}(\alpha)$ between zero and one in order to minimize both functions simultaneously by minimizing the loss function

$$\mathcal{L}^{\alpha} = \overline{\epsilon_{R_{rs}}(\alpha)} + \overline{\epsilon_{\delta_{\text{obla}}}(\alpha)},\tag{B1}$$

where the line over the errors stand for the re-scaling stands for the rescaling. Figure B1 shows the final value of α selected, as a function of $\epsilon_{R_{rs}}(\alpha)$, $\epsilon_{\delta_{chla}}(\alpha)$ and \mathcal{L}^{α} .

Appendix C

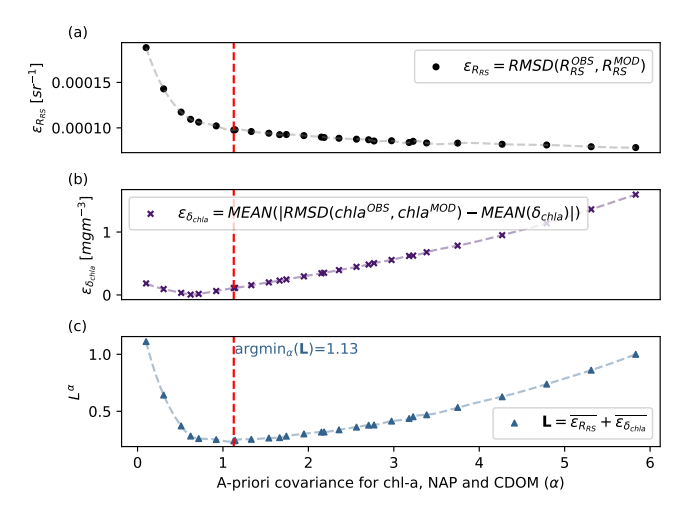


Figure B1. Illustration of how the hyper-parameter α was chosen. Using a higher α decreases the Root Mean Square Difference between the Remote Sensing Reflectance observed by satellite, and the one obtained with the model (a), but increases the error between the predicted uncertainty and the actual discrepancy between model and data (b). The value chosen was the one that minimized the \mathcal{L}^{α} loss function (c).

In this section, we show This section shows that \mathcal{L}_{ELBO} is a lower bound of the data log-likelihood, first, First, we write the expression for the log-likelihood, by marginalizing over all possible values of the latent variable z

750
$$\underline{\log(p_{\Lambda}(y))}\underline{\log(p_{\Lambda}(y))} = \log\left(\int_{\mathcal{Z}} p_{\Lambda}(y|z)p(z)dz\right),$$
 (C1)

next we introduce the parameterized probability distribution $q_{\phi}(z|y)$

$$= \log \left(\int_{\mathcal{Z}} p_{\Lambda}(\boldsymbol{y}|z) \frac{q_{\phi}(z|\boldsymbol{y})}{q_{\phi}(z|\boldsymbol{y})} p(z) dz \right), \tag{C2}$$

finally Finally, we use Jensen's inequality to find a lower bound of for the log-likelihood,

$$\geq \int_{\mathcal{Z}} \log \left(\frac{p_{\Lambda}(\boldsymbol{y}|z)p(z)}{q_{\phi}(z|\boldsymbol{y})} \right) q_{\phi}(z|\boldsymbol{y}) dz$$

$$= \int_{\mathcal{Z}} \log \left(\frac{p(z)}{q_{\phi}(z|\boldsymbol{y})} \right) q_{\phi}(z|\boldsymbol{y}) + \int_{\mathcal{Z}} \log (p_{\Lambda}(\boldsymbol{y}|z)) q_{\phi}(z|\boldsymbol{y}) dz$$

$$= -D_{KL}(q_{\phi}(z|\boldsymbol{y})||p(z)) + \mathbb{E}_{q_{\phi}(z|\boldsymbol{y})}[\log (p_{\Lambda}(\boldsymbol{y}|z))]$$

$$= \mathcal{L}_{ELBO}, \qquad (C3)$$

755 The inequality is an equality for the case $q_{\phi}(z|\boldsymbol{y}) = p(z|\boldsymbol{y})$, the true posterior distribution, in which case $\mathcal{L}_{ELBO} = \log(p_{\Lambda}(\boldsymbol{y}))$. In other words, maximising the \mathcal{L}_{ELBO} equals maximising the marginal log-likelihood.

Appendix D

760

In this section, we include the Root Mean Square Error (RMSE), Pearson correlation coefficients (ρ), and relative Median Absolute Deviation (rMAD) for all the measurements and observations, using the MAP estimates with unperturbed parameters, MAP estimate with parameters from the SGVB frameworkestimator, and outputs from the SGVB frameworkestimator. All the quantities are computed using only the test data, which is the 10% of the datathat was, not used in the MCMC algorithm nor or in the training of the neural network. We also include supplementary figures, with the 2012 timelines comparing the historical data with the output of the MAP estimates and the SGVB framework. Finally, we include tables with the symbols used across this work.

Table D1. Root Mean Square Error between satellite and in-situ observations, and the modeled data using the Maximum A-posterior (MAP) estimate with unperturbed parameters, optimized parameters with the MCMC algorithm, optimized parameters with the SGVB <u>based</u> framework, and modeled data purely with the SGVB <u>based</u> framework. Notice that a log transform was performed before the computations.

	MAP with unper-	$\frac{\text{RMSE(OBS,MOD)} = \sqrt{\text{MEAN}((\text{OBS} - \text{MOD})^2)}}{\text{MAP with MCMC pa}}$	MAP with SGVB pa-	·
		•	•	SGVB output
	turbed parameters	rameters	rameters	
$R_{RS,412.5}$	0.000319 <u>0.039998</u>	0.000151 - 0.040920	$0.000218 \cdot 0.042113$	0.000646-0.128636
$R_{RS,442.5}$	0.000117 - 0.019901	0.000115 - 0.022441	0.000120 + 0.019984	0.000553_0.117474
$R_{RS,490}$	0.000246_0.033773	0.000062 - 0.023230	0.000090 0.029305	0.000413-0.071944
$R_{RS,510}$	0.000078-0.033258	0.000065-0.038340	0.000108-0.039021	0.000242-0.059382
$R_{RS,555}$	$\underbrace{0.000067}_{0.019328}$	0.000046 - 0.031546	0.000044-0.033822	0.000191-0.091312
$k_{d,412.5}$	$\underbrace{0.044358}_{0.395717}$	0.044922 - 0.419141	0.048587-0.378790	0.049591-0.429363
$k_{d,442.5}$	0.031283-0.327759	0.028478 0.322888	0.031518-0.303636	0.033641-0.365043
$k_{d,490}$	0.026799-0.324604	0.023269-0.300414	0.025459 0.299151	0.026724_0.339610
$k_{d,510}$	0.021233 0.221749	0.018798 0.210633	0.020363_0.213028	0.020633-0.214196
$k_{d,555}$	0.014163 <u>0.135205</u>	0.013240 <u>0.130366</u>	0.013648 0.133158	0.014121 <u>0.137648</u>
$b_{b,p,442.5}$	0.000811_0.457789	0.000680 0.334198	0.000549 0.512618	0.000561-0.787984
$b_{b,p,490}$	0.000640 0.446384	0.000609 0.506215	0.000650 0.405386	0.000694_0.549156
$b_{b,p,555}$	0.000497_0.439231	0.000480 0.521719	0.000551-0.423929	0.000570 0.550503
chla	0.406792 <u>0.603652</u>	0.334460 0.587130	0.299325 0.502672	0.274626_0.447947
Total	0.547403.49835	0.46537 3.48918	0.441233.33661	0.42321-4.29020

The 2012 time series for the chlorophyll-α (a), Non-Algal Particles (b) and Chromophoric Dissolved Organic Matter (c). For all the timelines, the black points are the in-situ observations from the BOUSSOLE buoy, the blue points are the MAP output with uncertainty (blue shadow), using the optimal parameters from the SGVB framework algorithm, and the red points are the output of the SGVB framework.

Table D2. Pearson correlation coefficient *r* between satellite and in-situ observations, and the modeled data using the Maximum A-posterior (MAP) estimate with unperturbed parameters, optimized parameters with the MCMC algorithm, optimized parameters with the SGVB framework, and modeled data purely with the SGVB framework.

	Spearman rank-order correlation coefficient ρ			
	MAP with unper- turbed parameters	MAP with MCMC parameters	MAP with SGVB parameters	SGVB output
$R_{RS,412.5}$	0.98340_0.99304	0.99730_0.98841	0.99065_0.99041	0.96225_0.98306
$R_{RS,442.5}$	0.99710_0.99851	0.99863_0.99747	0.99738_ 0.99801_	0.97320 0.99192
$R_{RS,490}$	0.98461 <u>0.99715</u>	0.99737_0.99622	0.99604_0.99479	0.94149_0.98670
$R_{RS,510}$	0.98336_0.99201	0.99061_0.99105	0.97535_0.97962	0.79347_0.94380
$R_{RS,555}$	0.97605 <u>0.99378</u>	0.99331_0.99142	0.98685_0.97987	0.81142_0.92020
$k_{d,412.5}$	0.79925 <u>0.80801</u>	0.80544_0.81693	0.80709_0.81097	0.80948 0.81300
$k_{d,442.5}$	0.88829 0.88324	0.87788 <u>0.88525</u>	0.88310_0.88408	0.86992_0.87611
$k_{d,490}$	0.84538_0.84371	$0.84020 \cdot 0.85139$	0.84458_0.85001	0.83217_0.84049
$k_{d,510}$	0.85079 <u>0.85792</u>	0.85049 0.86398	0.85378 <u>0.86020</u>	0.83961_0.85466
$k_{d,555}$	0.66704_0.71051	0.63792_0.69352	0.66600 0.68246	0.63839 0.68541
$b_{b,p,442.5}$	0.65712-0.65502	0.68309 0.67547	0.70253_0.68759	0.70185_0.68896
$b_{b,p,490}$	0.53494_0.52632	0.59123 <u>0.57810</u>	0.61175_0.61910	0.63218_0.61431
$b_{b,p,555}$	0.65638-0.65197	0.68457 - 0.67520	0.69387_0.68754	0.69072_0.68674
chla	0.70004_0.85199	0.83500 0.86955	0.85845_0.87259	0.88942_0.87400
Total	11.52375 11.76319	11.78302 11.87396	11.86742 11.89723	11.38557 -11.75935

The 2012 time series for downward light attenuation coefficient $(k_d(\lambda))$, wavelengths $\lambda = 412.5$ (a), $\lambda = 442.5$ (b), $\lambda = 490$ (c), $\lambda = 510$ (d) and $\lambda = 555$ (e). For all the timelines, the black points are the in-situ observations from the BOUSSOLE buoy, the blue points are the MAP output with uncertainty (blue shadow), using the optimal parameters from the SGVB framework algorithm, and the red points are the output of the SGVB framework.

The 2012 time series for particulate backward scattering coefficient for the wavelengths λ = 442.5 (a), λ = 490 (b) and λ = 555 (c). For all the timelines, the black points are the in-situ observations from the BOUSSOLE buoy, the blue points are the MAP output with uncertainty (blue shadow), using the optimal parameters from the SGVB framework algorithm, and the red points are the output of the SGVB framework.

Table D3. relative Median Absolute Deviation (rMAD) between satellite and in-situ observations, and the modeled data using the Maximum A-posterior (MAP) estimate with unperturbed parameters, optimized parameters with the MCMC algorithm, optimized parameters with the SGVB framework, and modeled data purely with the SGVB framework.

	rMAD = MEAN(OBS - MOD /OBS)			
	MAP with unper-	MAP with MCMC pa-	MAP with SGVB pa-	SGVB output
	turbed parameters	rameters	rameters	SG v B output
$R_{RS,412.5}$	0.046498_0.029481	0.022824 0.031956	0.023695 0.032869	0.104053_0.122038
$R_{RS,442.5}$	$\underbrace{0.019152}_{0.014825} \underbrace{0.014825}_{}$	0.020253 0.016953	0.018087 <u>0.014725</u>	0.092863 <u>0.110805</u>
$R_{RS,490}$	$\underbrace{0.048393}_{0.028941}\underbrace{0.028941}_{}$	0.012281 <u>0.018827</u>	0.017828 0.024378	0.084470_0.066319
$R_{RS,510}$	0.022621_0.029412	0.019014_0.034112	$0.027908 \cdot 0.031342$	0.056772_0.046536
$R_{RS,555}$	$\underbrace{0.028433}_{0.015851}\underbrace{0.015851}_{}$	0.023294 0.025844	0.018036 0.022127	0.085871 <u>0.071504</u>
$k_{d,412.5}$	0.275663 <u>0.267226</u>	0.277158 0.284409	0.307413_0.262888	0.319424-0.270284
$k_{d,442.5}$	0.238534_0.226699	0.230608 0.224069	0.243371-0.219680	0.291961-0.245279
$k_{d,490}$	0.240852-0.222441	0.220262 0.212747	0.229272 0.214475	0.253470 0.228192
$k_{d,510}$	0.175974 0.168964	0.180554 0.167468	0.176727 - <u>0.169385</u>	0.176630 0.159414
$k_{d,555}$	$\underbrace{0.106287}_{0.101646}\underbrace{0.101646}_{0.106287}$	0.106784_0.100650	0.104700 <u>0.101680</u>	0.105321 - <u>0.101663</u>
$b_{b,p,442.5}$	0.350718 <u>0.316195</u>	0.285072-0.256815	0.244496 0.350178	0.259961-0.509545
$b_{b,p,490}$	$\underbrace{0.345372}_{0.376320}$	0.399523 0.556826	0.545586 0.311682	0.505087 <u>0.317715</u>
$b_{b,p,555}$	0.371178 <u>0.384337</u>	0.410633_0.568183	0.578075 0.365311	0.573776-0.379714
chla	0.552390 <u>0.725247</u>	0.572383 0.694534	0.474861_0.488889	0.283325 <u>0.305717</u>
Total	2.82207 2.90758	2.78064 3.19339	3.01006 2.60961	3.19298- 2.93472

Table D4. Table of Symbols used for the Radiative Transfer Model.

Symbol	Meaning	
$E_{ m dir}$	Vertical Direct irradiance	
$E_{ m dif}$	Vertical scattered downward irradiance	
E_{u}	Vertical scattered upward irradiance	
θ	Sun zenith angle	
h	depth at which a measurement is assumed to be taken.	
λ	Wavelength at which a measurement is assumed to be taken.	
$a(\lambda)$	Total absorption coefficient	
$b(\lambda)$	Total scattering coefficient	
$b_b(\lambda)$	Total backward scattering coefficient	
W	Water	
phy	Phytoplankton	
chla	Chlorophyll- α	
CDOM	Chromophoric Dissolved Organic Matter	
NAP	Non Algal Particles	
$a_{\mathrm{w}}(\lambda)$	Water-specific absorption coefficient	
$a_{ ext{phy}}(\lambda)$	Chlorophyll-specific absorption coefficient of phytoplankton	
$a_{ ext{CDOM}}(\lambda)$	Mass-specific absorption coefficient of CDOM	
$a_{ ext{NAP}}(\lambda)$	Mass-specific absorption coefficient of NAP	
$b_{ m w}(\lambda)$	Water-specific scattering coefficient	
$b_{ ext{phy}}(\lambda)$	Carbon-specific scattering coefficient of phytoplankton	
$b_{ ext{NAP}}(\lambda)$	Mass-specific scattering coefficient of NAP	
$b_{b,\mathrm{w}}(\lambda)$	Water-specific backward scattering coefficient	
$b_{b,\mathrm{phy}}(\lambda)$	Carbon-specific backward scattering coefficient of phytoplankton	
$b_{b, ext{NAP}}(\lambda)$	Mass-specific backward scattering coefficient of NAP	
PAR	Photosynthetic Available Radiation	
$E_{\rm dir}^{\rm OASIM}(0,\lambda)$	Direct downward irradiance on the surface of the ocean, from the OASIM model	
$E_{\rm dif}^{\rm OASIM}(0,\lambda)$	Scattered downward irradiance on the surface of the ocean, from the OASIM model	
$E_{\mathrm{u}}(\infty,\lambda)$	Scattered upward irradiance on the floor of the ocean	
R_{rs}	Remote Sensing Reflectance	
$b_{b,p}$	Particulate backward scattering coefficient	
k_d	Downward light attenuation coefficient	

Table D5. Table of Symbols and notation used for the Bayes formalism.

Symbol	Meaning	
y	Vector, discretization of a continuous function in discrete values of λ	
y_{λ}	Component of a vector with magnitude $y(\lambda)$	
z^*	Optimal value of a retrieved quantity z , solution of a minimization problem	
\hat{z}	Estimation of the optimal value of a quantity z	
$\mathrm{argmin}_z \mathcal{L}(z)$	Quantity z that minimized the loss function ${\cal L}$	
$\operatorname{argmax}_z p(y z)$	Quantity z that maximises the likelihood $p(y z)$	
$oldsymbol{y}^d$	Remote Sensing Reflectance data from day d	
x^d	OASIM data from day d	
z^d	Optical constituents from day d	
Λ	Set of parameters from the forward model	
Y	Set of many days with Remote Sensing Reflectance data, which represents the train set when is	
	used for training, and the test set when is used for testing	
X	Set of many days with OASIM data, which represents the train set when is used for training, and	
	the test set when is used for testing	
Z	Set of many days with retrieved optical constituents, which represents the train set when is used	
	for training, and the test set when is used for testing	
$p_{\Lambda}(oldsymbol{y} z,oldsymbol{x})$	Probability distribution of the variable y conditional on z , and x , as a function of Λ	
$\mathcal{N}(\mu, \Sigma)$	Gaussian probability distribution with mean μ and covariance matrix Σ	
H^{OBS}	in-situ observations	
$H^{ ext{MODEL}}$	Model of the in-situ observations	
\mathcal{H}	Observation operator, equal to H^{OBS} when there were observations, and zero otherwise	
I^d	Presence-absence nine dimension indicator function	
\mathcal{L}^H	Loss function used to minimize the distance between in-situ observations and predicted obse	
	tions	
\mathcal{L}^z	Loss function used to maximize the posterior probability $p_{\Lambda}(\tilde{z}^d \boldsymbol{y}^d,\boldsymbol{x}^d)$ for every day d	
$ ilde{z}$	optical constituents with the change of variable $\tilde{z} = \log(z)$	
Σ_{ϵ}	Covariance matrix of the Remote Sensing Reflectance	
ϵ	Noise of the Remote Sensing Reflectance	
δ_{Λ}	Perturbations on the parameters	
$ abla_{ ilde{z}^d}$	Gradient over every component of $ ilde{z}^d$	
Σ_z	Covariance of the prior term associated to the optical constituents $\Sigma_z = \alpha \mathbb{1}$, $\mathbb{1}$ the identity matrix	

Table D6. Table of Symbols and notation notations used for the SGVB Variational Bayes formalism.

Symbol	Meaning	
Z	Latent variable sampled from an unknown distribution $p_{\Lambda^*}(z)$	
y	Random variable sampled from a known conditional distribution $p_{\Lambda^*}(\boldsymbol{y} z)$	
$p_{\Lambda}(y)$	data-Likelihood of the parameter Λ	
$p_{\Lambda}(z oldsymbol{y})$	Posterior probability of the latent variable z	
$q_{\phi}(z oldsymbol{y})$	Estimate of the posterior probability of the latent variable z	
\mathcal{L}_{ELBO}	ELBO loss function, where ELBO stands for "Evidence Lower Bound"	
$D_{KL}(q_{\phi}(z oldsymbol{y}) p_{\Lambda}(z))$	Kullback-Leibler divergence between the two probability distributions $q_{\phi}(z oldsymbol{y})$ and	
	$p_{\Lambda}(z)$	
$\mathbb{E}_{q_{oldsymbol{\phi}}(z oldsymbol{y})}[log(p_{\Lambda}(oldsymbol{y} z))]$	Expected value of $log(p_{\Lambda}(\boldsymbol{y} z))$ with respect to the probability distribution $q_{\phi}(z \boldsymbol{y})$	

Author contributions. CS implemented the code, performed the experiments, and wrote the first draft of the manuscript, MGDK did the data processing. PL and FA supervised the work. All authors collaborated on the design of the models and contributed to the manuscript's writing.

Competing interests. The contact author has declared that none of the authors has any competing interests.

780 fFinancia supporThis research has been supported by the European Commission HORIZON EUROPE Framework Programme (grant no. 101081273).

This research has been partly supported by the MED-MFC (Mediterranean – Monitoring Forecasting Centre) of the Copernicus Marine Service, which is implemented by Mercator Ocean International within the framework of a delegation agreement with the European Union (reference no. 21002L5-COP-MFC MED-5500).

785 *Financial support.* This research has been supported by the European Commission HORIZON EUROPE Framework Programme (grant no. 101081273).

This research has been partly supported by the MED-MFC (Mediterranean – Monitoring Forecasting Centre) of the Copernicus Marine Service, which is implemented by Mercator Ocean International within the framework of a delegation agreement with the European Union (reference no. 21002L5-COP-MFC MED-5500).

790 References

795

- Aas, E.: Two-stream irradiance model for deep waters, Applied Optics, 26, 2095–2101, 1987.
- Aas, E. and Højerslev, N. K.: Analysis of underwater radiance observations: Apparent optical properties and analytic functions describing the angular radiance distribution, Journal of Geophysical Research: Oceans, 104, 8015–8024, 1999.
- Ackleson, S. G., Balch, W. M., and Holligan, P. M.: Response of water-leaving radiance to particulate calcite and chlorophyll a concentrations: A model for Gulf of Maine coccolithophore blooms, Journal of Geophysical Research: Oceans, 99, 7483–7499, 1994.
- Álvarez, E., Cossarini, G., Teruzzi, A., Bruggeman, J., Bolding, K., Ciavatta, S., Vellucci, V., d'Ortenzio, F., Antoine, D., and Lazzari, P.: Chromophoric dissolved organic matter dynamics revealed through the optimization of an optical-biogeochemical model in the NW Mediterranean Sea, Biogeosciences Discussions, 2023, 1–43, 2023.
- Andrieu, C. and Thoms, J.: A tutorial on adaptive MCMC, Statistics and computing, 18, 343-373, 2008.
- Antoine, D., Guevel, P., Deste, J.-F., Becu, G., Louis, F., Scott, A. J., and Bardey, P.: The "BOUSSOLE" buoy—A new transparent-to-swell taut mooring dedicated to marine optics: Design, tests, and performance at sea, Journal of Atmospheric and Oceanic Technology, 25, 968–989, 2008.
 - Arras, K. O.: An introduction to error propagation: derivation, meaning and examples of equation CY= FX CX FXT, Tech. rep., ETH Zurich, 1998.
- 805 Barron, J. T.: Continuously differentiable exponential linear units, arXiv preprint arXiv:1704.07483, 2017.
 - Barthélémy, S., Brajard, J., Bertino, L., and Counillon, F.: Super-resolution data assimilation, Ocean Dynamics, 72, 661-678, 2022.
 - Bocquet, M., Brajard, J., Carrassi, A., Bertino, L., et al.: Bayesian inference of chaotic dynamics by merging data assimilation, machine learning and expectation-maximization, FOUNDATIONS OF DATA SCIENCE, 2, 55–80, 2020.
- Bodin, N., Burgeot, T., Stanisiere, J., Bocquené, G., Menard, D., Minier, C., Boutet, I., Amat, A., Cherel, Y., and Budzinski, H.: Seasonal variations of a battery of biomarkers and physiological indices for the mussel Mytilus galloprovincialis transplanted into the northwest Mediterranean Sea, Comparative Biochemistry and Physiology Part C: Toxicology & Pharmacology, 138, 411–427, 2004.
 - Boehme, L. and Rosso, I.: Classifying oceanographic structures in the Amundsen Sea, Antarctica, Geophysical Research Letters, 48, e2020GL089412, 2021.
- Boynton, G. C. and Gordon, H. R.: Irradiance inversion algorithm for estimating the absorption and backscattering coefficients of natural waters: Raman-scattering effects, Applied Optics, 39, 3012–3022, 2000.
 - Brajard, J., Jamet, C., Moulin, C., and Thiria, S.: Use of a neuro-variational inversion for retrieving oceanic and atmospheric constituents from satellite ocean colour sensor: Application to absorbing aerosols, Neural Networks, 19, 178–185, 2006.
 - Brankart, J.-M., Testut, C.-E., Béal, D., Doron, M., Fontana, C., Meinvielle, M., Brasseur, P., and Verron, J.: Towards an improved description of ocean uncertainties: effect of local anamorphic transformations on spatial correlations, Ocean Science, 8, 121–142, 2012.
- Bruggeman, J., Bolding, K., Nerger, L., Teruzzi, A., Spada, S., Skákala, J., and Ciavatta, S.: EAT v0. 9.6: a 1D testbed for physical-biogeochemical data assimilation in natural waters, Geoscientific Model Development Discussions, 2023, 1–22, 2023.
 - Campbell, J. W.: The lognormal distribution as a model for bio-optical variability in the sea, Journal of Geophysical Research: Oceans, 100, 13 237–13 254, 1995.
- Carmichael, G. R., Sandu, A., et al.: Sensitivity analysis for atmospheric chemistry models via automatic differentiation, Atmospheric Environment, 31, 475–489, 1997.

- Chapman, C. and Charantonis, A. A.: Reconstruction of subsurface velocities from satellite observations using iterative self-organizing maps, IEEE Geoscience and Remote Sensing Letters, 14, 617–620, 2017.
- Chib, S. and Greenberg, E.: Understanding the metropolis-hastings algorithm, The american statistician, 49, 327–335, 1995.
- CMEMS: Mediterranean Sea, Bio-Geo-Chemical, L3, daily Satellite Observations (1997-ongoing). E.U. Copernicus Marine Service Information (CMEMS), doi: https://doi.org/10.48670/moi-00299, (Accessed on 11-13-2023).
 - Colella, S., Brando, V. E., Cicco, A. D., D'Alimonte, D., Forneris, V., and Bracaglia, M.: Ocean Colour Mediterranean and Black Sea Observation Product, ref: CMEMS-OC-QUID-009-141to144-151to154, url: https://catalogue.marine.copernicus.eu/documents/QUID/CMEMS-OC-QUID-009-141to144-151to154.pdf, 2023.
- Colella, S., Brando, V, E., Di Cicco, A., D'Alimonte, D., Forneris, V., and Bracaglia, M.: EU Copernicus Marine Service Quality Information

 Document for the Ocean Colour Mediterranean and Black Sea Observation Product, OCEANCOLOUR_MED_BGC_L3_NRT_009_143,

 Issue 4.1, Mercator Ocean International, https://doi.org/10.48670/moi-00299, (Accessed on 05-23-2025), 2025.
 - Cramér, H.: Mathematical methods of statistics, vol. 9, Princeton university press, 1999.
 - De Bézenac, E., Pajot, A., and Gallinari, P.: Deep learning for physical processes: Incorporating prior scientific knowledge, Journal of Statistical Mechanics: Theory and Experiment, 2019, 124 009, 2019.
- Denvil-Sommer, A., Gehlen, M., Vrac, M., and Mejia, C.: LSCE-FFNN-v1: a two-step neural network model for the reconstruction of surface ocean p CO 2 over the global ocean, Geoscientific Model Development, 12, 2091–2105, 2019.
 - Desbruyères, D., Chafik, L., and Maze, G.: A shift in the ocean circulation has warmed the subpolar North Atlantic Ocean since 2016, Communications Earth & Environment, 2, 48, 2021.
- Dessailly, D.: Retrieval of the spectral diffuse attenuation coefficient Kd (λ) in open and coastal ocean waters using a neural network inversion, Journal of Geophysical Research: Oceans, 117, 2012.
 - Di Biagio, V., Campanella, S., and Cossarini, G.: In situ dataset for initialization and validation of the Copernicus Med-MFC biogeochemical model system (MedBGCins), https://doi.org/10.5281/zenodo.15489967, 2025.
 - Doersch, C.: Tutorial on Variational Autoencoders, 2021.
- Dutkiewicz, S., Hickman, A., Jahn, O., Gregg, W., Mouw, C., and Follows, M.: Capturing optically important constituents and properties in a marine biogeochemical and ecosystem model, Biogeosciences, 12, 4447–4481, 2015.
 - Erichson, N. B., Muehlebach, M., and Mahoney, M. W.: Physics-informed autoencoders for Lyapunov-stable fluid flow prediction, arXiv preprint arXiv:1905.10866, 2019.
 - Erickson, Z. K., McKinna, L., Werdell, P. J., and Cetinić, I.: Bayesian approach to a generalized inherent optical property model, Optics Express, 31, 22790–22801, 2023.
- Falkner, S., Klein, A., and Hutter, F.: BOHB: Robust and efficient hyperparameter optimization at scale, in: International conference on machine learning, pp. 1437–1446, PMLR, 2018.
 - Geider, R., MacIntyre, H., and Kana, T.: Dynamic model of phytoplankton growth and acclimation: responses of the balanced growth rate and the chlorophyll a: carbon ratio to light, nutrient-limitation and temperature, Marine Ecology Progress Series, 148, 187–200, 1997.
- George, T. M., Manucharyan, G. E., and Thompson, A. F.: Deep learning to infer eddy heat fluxes from sea surface height patterns of mesoscale turbulence, Nature communications, 12, 800, 2021.
 - Gordon, H. R.: Inverse methods in hydrologic optics, Oceanologia, 44, 2002.
 - Gordon, H. R. and Boynton, G. C.: Radiance—irradiance inversion algorithm for estimating the absorption and backscattering coefficients of natural waters: homogeneous waters, Applied optics, 36, 2636–2641, 1997.

- Gregg, W. W. and Casey, N. W.: Skill assessment of a spectral ocean–atmosphere radiative model, Journal of Marine Systems, 76, 49–63, 2009.
 - Ham, Y.-G., Kim, J.-H., and Luo, J.-J.: Deep learning for multi-year ENSO forecasts, Nature, 573, 568-572, 2019.
 - Irrgang, C., Saynisch, J., and Thomas, M.: Estimating global ocean heat content from tidal magnetic satellite observations, Scientific Reports, 9, 7893, 2019.
 - Jones, D. and Ito, T.: Gaussian mixture modeling describes the geography of the surface ocean carbon budget., 2019.
- 870 Jones, D. C., Holt, H. J., Meijers, A. J., and Shuckburgh, E.: Unsupervised clustering of Southern Ocean Argo float temperature profiles, Journal of Geophysical Research: Oceans, 124, 390–402, 2019.
 - Kingma, D. P. and Welling, M.: Auto-encoding variational bayes, arXiv preprint arXiv:1312.6114, 2013.
 - Lachkar, Z. and Gruber, N.: A comparative study of biological production in eastern boundary upwelling systems using an artificial neural network, Biogeosciences, 9, 293–308, 2012.
- Lazzari, P., Solidoro, C., Ibello, V., Salon, S., Teruzzi, A., Béranger, K., Colella, S., and Crise, A.: Seasonal and inter-annual variability of plankton chlorophyll and primary production in the Mediterranean Sea: a modelling approach, Biogeosciences, 9, 217–233, 2012.
 - Lazzari, P., Salon, S., Terzić, E., Gregg, W. W., d'Ortenzio, F., Vellucci, V., Organelli, E., and Antoine, D.: Assessment of the spectral downward irradiance at the surface of the Mediterranean Sea using the OASIM ocean-atmosphere radiative model, Ocean Science Discussions, 2020, 1–39, 2020.
- Lazzari, P., dit Kacem, G., M, A. E., Chernov, I., and Vellucci, V.: Determination of Biogeochemical Properties in Sea Waters Using the Inversion of the Three-stream Irradiance Model, Scientific Reports, https://doi.org/https://doi.org/10.1038/S41598-024-71457-5, 2024.
 - Leathers, R. A., Roesler, C. S., and McCormick, N. J.: Ocean inherent optical property determination from in-water light field measurements, Applied Optics, 38, 5096–5103, 1999.
- Lee, Z., Carder, K. L., and Arnone, R. A.: Deriving inherent optical properties from water color: a multiband quasi-analytical algorithm for optically deep waters, Applied optics, 41, 5755–5772, 2002.
 - Liaw, R., Liang, E., Nishihara, R., Moritz, P., Gonzalez, J. E., and Stoica, I.: Tune: A research platform for distributed model selection and training, arXiv preprint arXiv:1807.05118, 2018.
 - Longhurst, A., Sathyendranath, S., Platt, T., and Caverhill, C.: An estimate of global primary production in the ocean from satellite radiometer data, Oceanographic Literature Review, 2, 203, 1996.
- Manucharyan, G. E., Siegelman, L., and Klein, P.: A deep learning approach to spatiotemporal sea surface height interpolation and estimation of deep currents in geostrophic ocean turbulence, Journal of Advances in Modeling Earth Systems, 13, e2019MS001 965, 2021.
 - Martinez, E., Gorgues, T., Lengaigne, M., Fontana, C., Sauzède, R., Menkes, C., Uitz, J., Di Lorenzo, E., and Fablet, R.: Reconstructing global chlorophyll-a variations using a non-linear statistical approach, Frontiers in Marine Science, 7, 464, 2020.
 - Mason, J. D., Cone, M. T., and Fry, E. S.: Ultraviolet (250–550 nm) absorption spectrum of pure water, Applied optics, 55, 7163–7172, 2016.
- Maze, G., Mercier, H., Fablet, R., Tandeo, P., Radcenco, M. L., Lenca, P., Feucher, C., and Le Goff, C.: Coherent heat patterns revealed by unsupervised classification of Argo temperature profiles in the North Atlantic Ocean, Progress in Oceanography, 151, 275–292, 2017.
 - McCormick, N.: Analytical transport theory applications in optical oceanography, Annals of Nuclear Energy, 23, 381–395, 1996.
 - Michalopoulou, Z.-H., Bagheri, S., and Axe, L.: Bayesian estimation of optical properties of nearshore estuarine waters: A Gibbs sampling approach, IEEE transactions on geoscience and remote sensing, 48, 1579–1587, 2009.
- 900 Mignot, A., Claustre, H., D'Ortenzio, F., Xing, X., Poteau, A., and Ras, J.: From the shape of the vertical profile of in vivo fluorescence to Chlorophyll-a concentration, Biogeosciences, 8, 2391–2406, https://doi.org/10.5194/bg-8-2391-2011, 2011.

- Morel, A.: Optical properties of pure water and pure sea water, Optical Aspects of Oceanography, 1, 1974.
- Mustapha, Z. B., Alvain, S., Jamet, C., Loisel, H., and Dessailly, D.: Automatic classification of water-leaving radiance anomalies from global SeaWiFS imagery: application to the detection of phytoplankton groups in open ocean waters, Remote sensing of environment, 146, 97–112, 2014.
 - Paszke, A., Gross, S., Massa, F., Lerer, A., Bradbury, J., Chanan, G., Killeen, T., Lin, Z., Gimelshein, N., Antiga, L., Desmaison, A., Kopf, A., Yang, E., DeVito, Z., Raison, M., Tejani, A., Chilamkurthy, S., Steiner, B., Fang, L., Bai, J., and Chintala, S.: PyTorch: An Imperative Style, High-Performance Deep Learning Library, arXiv preprint arXiv:1912.01703, 2019.
- Pietropolli, G., Cossarini, G., and Manzoni, L.: GANs for integration of deterministic model and observations in marine ecosystem, in: EPIA Conference on Artificial Intelligence, pp. 452–463, Springer, 2022.
 - Richardson, A. J., Risien, C., and Shillington, F. A.: Using self-organizing maps to identify patterns in satellite imagery, Progress in Oceanography, 59, 223–239, 2003.
 - Rodgers, C. D.: Inverse methods for atmospheric sounding: theory and practice, vol. 2, World scientific, 2000.
 - Ronald, J. and Zaneveld, V.: Remotely sensed reflectance and its dependence on vertical structure: a theoretical derivation, Applied Optics, 21, 4146–4150, 1982.
 - Salama, M. S. and Verhoef, W.: Two-stream remote sensing model for water quality mapping: 2SeaColor, Remote sensing of Environment, 157, 111–122, 2015.
 - Saraceno, M., Provost, C., and Lebbah, M.: Biophysical regions identification using an artificial neuronal network: A case study in the South Western Atlantic, Advances in Space Research, 37, 793–805, 2006.
- 920 Shlens, J.: Notes on kullback-leibler divergence and likelihood, arXiv preprint arXiv:1404.2000, 2014.

915

- Shmakov, A., Greif, K., Fenton, M., Ghosh, A., Baldi, P., and Whiteson, D.: End-To-End Latent Variational Diffusion Models for Inverse Problems in High Energy Physics, Advances in Neural Information Processing Systems, 36, 2024.
- Simpson, J. and Dickey, T.: The relationship between downward irradiance and upper ocean structure, Journal of Physical Oceanography, 11, 309–323, 1981.
- 925 Sohn, K., Lee, H., and Yan, X.: Learning structured output representation using deep conditional generative models, Advances in neural information processing systems, 28, 2015.
 - Soto, C.: Data-Informed Inversion Model (DIIM), https://doi.org/10.5281/zenodo.14609747, 2025.
 - Stramska, M., Stramski, D., Mitchell, B. G., and Mobley, C. D.: Estimation of the absorption and backscattering coefficients from in water radiometric measurements, Limnology and Oceanography, 45, 628–641, 2000.
- 930 Tao, Z., McCormick, N. J., and Sanchez, R.: Ocean source and optical property estimation from explicit and implicit algorithms, Applied Optics, 33, 3265–3275, 1994.
 - Van Rossum, G. and Drake, F. L.: Introduction to python 3: python documentation manual part 1, CreateSpace, 2009.
 - Virtanen, P., Gommers, R., Oliphant, T. E., Haberland, M., Reddy, T., Cournapeau, D., Burovski, E., Peterson, P., Weckesser, W., Bright, J., van der Walt, S. J., Brett, M., Wilson, J., Millman, K. J., Mayorov, N., Nelson, A. R. J., Jones, E., Kern, R., Larson, E., Carey, C. J., Polat,
- 935 İ., Feng, Y., Moore, E. W., VanderPlas, J., Laxalde, D., Perktold, J., Cimrman, R., Henriksen, I., Quintero, E. A., Harris, C. R., Archibald, A. M., Ribeiro, A. H., Pedregosa, F., van Mulbregt, P., and SciPy 1.0 Contributors: SciPy 1.0: Fundamental Algorithms for Scientific Computing in Python, Nature Methods, 17, 261–272, https://doi.org/10.1038/s41592-019-0686-2, 2020.
 - Zaneveld, J. R. V.: An asymptotic closure theory for irradiance in the sea and its inversion to obtain the inherent optical properties, Limnology and Oceanography, 34, 1442–1452, 1989.

- P40 Zhao, Z., Ye, J. C., and Bresler, Y.: Generative Models for Inverse Imaging Problems: From mathematical foundations to physics-driven applications, IEEE Signal Processing Magazine, 40, 148–163, 2023.
 - Zhong, E. D., Bepler, T., Davis, J. H., and Berger, B.: Reconstructing continuous distributions of 3D protein structure from cryo-EM images, arXiv preprint arXiv:1909.05215, 2019.
- Zhong, E. D., Lerer, A., Davis, J. H., and Berger, B.: Cryodrgn2: Ab initio neural reconstruction of 3d protein structures from real cryo-em images, in: Proceedings of the IEEE/CVF International Conference on Computer Vision, pp. 4066–4075, 2021.